

FINAL REPORT

for

Computer Simulation of Surface and Film Processes

November 1, 1984

Cooperative Agreement No.: NCC 2-125

Period of Award: May 1, 1981 - April 30, 1984

Principal Investigator: Professor W. A. Tiller

Senior Investigator: Dr. M. T. Halicioglu

(NASA-CR-176966) : COMPUTER SIMULATION OF  
SURFACE AND FILM PROCESSES Final Report, 1  
May 1981 - 30-Apr. 1984 (Stanford Univ.)  
75 p

N86-31377

CSCI 20L

Unclas  
G3/76 43016

SU-DMS-85-R-1

Stanford/NASA Ames Joint Institute for Surface and  
Microstructure Research  
Department of Materials Science and Engineering  
Stanford University, Stanford, CA 94305

## CHAPTER I

### Introduction

A detailed knowledge of the structure at an atomistic level is very important for understanding of various processes which take place at surfaces and interfaces. The exact geometry of different atomic configurations is needed for a correct interpretation of various experimental observations. In spite of the sophisticated experimental techniques available for examining surface structure and surface chemistry, many structure-related characteristics (e.g., surface reconstruction, catalysis) remain unresolved. Specific surface processes like catalysis, diffusion, roughening, wetting, adhesion, nucleation, crystal growth, crack propagation, corrosion, etc., are so complex that detailed understanding of surface structure is essential for understanding the key elements involved in the specific process. Unfortunately, conventional theoretical techniques have great difficulty in coping with the many "nested" phenomena involved in these processes at a detailed level.

Computer simulation techniques, on the other hand, employing advanced numerical methods and well-known statistical approaches, are now beginning to contribute significantly to the microscopic understanding of surfaces and ad-layer technology as well as to a better understanding of the atomic mechanisms involved in various materials surface-related processes [1,2].

The main issue in computer simulation is, of course, the ability to generate a mathematical description or a "model" that will accurately reflect what is happening in the real world. Prior to the advent of computer technology, applied mathematics provided a few situations which

could be described by analytically solvable equations. Unfortunately, important aspects of surface-related processes and materials behavior usually are complex phenomena which tend to be resistant to analytical treatment and even to definitive studies by laboratory experimental means. During the past decades, complex processes have been studied, with increasing frequency, using "computer simulation experiments." The results have been particularly useful and illuminating [1-3]. These simulation studies have motivated not only improved laboratory experiment designs but also have made possible improved data interpretation techniques.

The most important objective of this project was to acquire an atomic level information for different surface-related phenomena. This was accomplished using basically three different simulation techniques [4]. All the investigations which were carried out employed in one way or another a computer simulation technique based on atomistic level considerations. In general, three types of simulation methods are being used for modeling systems with discrete particles that interact via well defined potential functions.

- (i) Molecular dynamics: this is a general method for solving the classical equations of motion of a model system. It provides time evolution of a system of many particles. One can obtain pertinent phase space trajectories, therefore, any physical property can, in principle, be calculated if the system Hamiltonian is known. Given the initial position and velocity vectors for each particle, the dynamical history of the assembly is generated in the computer. The simultaneous equations of motion are solved by any of several techniques which

involve extrapolating the atomic trajectories over successive short time intervals. After each extrapolation the forces on all the particles are recalculated at their new positions, and the resulting accelerations used in the next extrapolation.

(ii) Monte-Carlo: in general, the term Monte-Carlo refers to the Markov chain ensemble averaging technique introduced by Metropolis et al. It is purely a stochastic method to model equilibrium properties of a system. Accordingly, Monte-Carlo methods cannot simulate atomic motions in real time, but generate a large number of configurations (i.e., snapshots of  $N$ -particle positions representative of an ensemble at  $T$ ). Equation of state data are obtained by appropriate averages over these generated configurations.

(iii) Molecular statics: this method, in principle, can only provide properties of a system at  $T = 0^\circ\text{K}$ . Its widespread use stems from its small demand of computer time and its ability to handle large systems. Molecular statics can be regarded as a minimization procedure. In general, the objective is to find the energetically most favorable configuration. It may be thought of as molecular dynamics with a damping force which progressively draws energy out of the system until it arrives at a configuration of stable static equilibrium (i.e., a minimum of the potential energy function). Frequently, molecular statics results are employed as starting configurations (i.e., as an input) in the Monte-Carlo and molecular dynamics calculations.

All three of these techniques are based on a well-defined potential function describing interactions among particles in the system.

In general, for a system of  $N$  particles, the total potential energy may be expanded as [5]:

$$\begin{aligned} \Phi = & \frac{1}{2!} \sum_i^N \sum_{j \neq i}^N u(\vec{r}_i, \vec{r}_j) + \frac{1}{3!} \sum_i^N \sum_{j \neq i}^N \sum_{k \neq i, j}^N u(\vec{r}_i, \vec{r}_j, \vec{r}_k) \\ & + \dots + \frac{1}{n!} \sum_i^N \sum_{j \neq i}^N \dots \sum_{k \neq i, j, \dots}^N u(\vec{r}_i, \vec{r}_j, \dots, \vec{r}_n) + \dots \end{aligned} \quad (1)$$

where,  $u(\vec{r}_i, \vec{r}_j)$ ,  $u(\vec{r}_i, \vec{r}_j, \vec{r}_k)$ , ...,  $u(\vec{r}_i, \vec{r}_j, \dots, \vec{r}_n)$  are two, three, and  $n$ -body potentials, respectively. The position of the  $i^{\text{th}}$  particle is denoted by  $\vec{r}_i$ .

Clearly, the most important term in this expansion is the first term involving two-body interactions. Therefore, in the majority of the atomistic calculations made to date, only pairwise additive potentials have been used. This provides great simplification in the analytical formalism as well as in numerical computations.

In this project, depending on the type of the system under consideration, the total potential energy  $\Phi$  was calculated either considering "only" a two-body term, or for more quantitative results it was calculated as a sum of two- and three-body interactions neglecting four- and higher-body terms in eq. (1). Because this expression (eq. (1)) had to be used in lengthy machine computations,  $u(\vec{r}_i, \vec{r}_j)$  and  $u(\vec{r}_i, \vec{r}_j, \vec{r}_k)$  were chosen with the simplest possible functional forms. In this study,

therefore, the two-body part was represented by a Mie-type potential which is given by:

$$u(r_{ij}) = \frac{\epsilon}{(m-n)} \left( n \left( \frac{r_0}{r_{ij}} \right)^m - m \left( \frac{r_0}{r_{ij}} \right)^n \right) \quad (2)$$

with  $r_{ij} = |\vec{r}_i - \vec{r}_j|$ ,  $r_0$  denotes the equilibrium separation and  $\epsilon$  is the energy at  $r_{ij} = r_0$ . The exponents  $m$  and  $n$  account for the repulsive and attractive terms, respectively. The three-body part, on the other hand, was expressed as:

$$u(\vec{r}_i, \vec{r}_j, \vec{r}_k) = \sum_{\lambda} Z_{\lambda} \cdot G_{\lambda}(\vec{r}_i, \vec{r}_j, \vec{r}_k) \quad (3)$$

where, the summation includes all triple multipole interactions resulting from the expansion of the third-order interaction energy for three atoms. Each term in the summation is expressed as the product of a geometrical factor  $G(\vec{r}_i, \vec{r}_j, \vec{r}_k)$  which depends on the relative positions of the three atomic nuclei and an interaction constant which depends only on the atomic species involved in the interaction. The functional forms of  $G(\vec{r}_i, \vec{r}_j, \vec{r}_k)$  for several multiple interactions have been obtained by Doren and Zucker [6]. Here, we consider only the triple-dipole interaction which has been shown to be the dominant contribution [7]. This term was first obtained for closed shell atoms as:

$$u(\vec{r}_i, \vec{r}_j, \vec{r}_k) = Z_1 \cdot G_1(\vec{r}_i, \vec{r}_j, \vec{r}_k) \quad (4)$$

with

$$G_1(r_i, r_j, r_k) = \frac{1 + 3 \cos \theta_i \cos \theta_j \cos \theta_k}{(r_{ij} \cdot r_{ik} \cdot r_{jk})^3} \quad (5)$$

where  $\theta_i, \theta_j, \theta_k$  and  $r_{ij}, r_{ik}, r_{jk}$  represent the angle and the sides of the triangle formed by the three particles  $i, j$  and  $k$ .

In general, model systems interacting only via two-body potentials have been used for parametrical analyses, or to obtain semi-qualitative results for resolving simple mechanisms at atomistic levels. While these two-body model potentials are able to reproduce characteristics of some systems (i.e., solid rare gases, fcc crystals, etc.), they are unable to simulate other systems with somewhat more complex structures (e.g., diamond, graphite structures). Therefore, for systems with more involved structures three-body interactions are included by combining eqs. (1) through (5). Accordingly, the total potential energy was expressed as:

$$\begin{aligned} \Phi = & \frac{1}{2} \sum_i \sum_j \frac{\epsilon}{(m-n)} \left( n \left( \frac{r_0}{r_{ij}} \right)^m - m \left( \frac{r_0}{r_{ij}} \right)^n \right) \\ & + \frac{1}{3!} \sum_i \sum_j \sum_k \frac{Z(1 + 3 \cos \theta_1 \cos \theta_2 \cos \theta_3)}{(r_{ij} \cdot r_{ik} \cdot r_{jk})^3} . \end{aligned} \quad (6)$$

This equation has been used earlier for other analyses, when the effect of three-body interactions on the structural characteristics of small clusters [8] and on various crystalline solids [5] were investigated. In these analyses the importance of the many-body effect has been clearly demonstrated. The function  $\Phi$  containing three-body interactions is able to provide stability regions for many different types of

crystalline materials [5]. In this project, to investigate the multi-body effect further, in Chapter II we analyze the effect of three-body forces on the vibrational frequencies of triatomic clusters. In another study, which is presented in Chapter III, the multilayer relaxation phenomena for low index planes of an fcc crystal was analyzed also as a function of the three-body interactions.

For the simulation of real systems, the energy parameters of eq. (6) are needed. Evaluation of these parameters is, in general, a cumbersome procedure which is outlined in Chapter IV along with the numerical values of the parameters for some selected compounds. In Chapter V various surface properties for Si and SiC systems are calculated.

The rest of the studies in this report are related to materials applications that involve analyses of responses of materials to external forces. In Chapter VI, results obtained from static simulation calculations for slip formation are presented, while in Chapter VII more elaborate molecular dynamics calculations on the propagation of cracks in two-dimensional systems are outlined.



## CHAPTER II

### The Effect of Three-body Forces on the Vibrational Frequencies of Triatomic Clusters

In general, experimental information about the energetics and structural characteristics of very small "isolated" clusters are obtained from various spectroscopic measurements [9-11]. Formal relationships between the observed spectral lines and the interatomic forces operational among the particles in the cluster are well established. From a knowledge of the interatomic potentials, for example, vibrational frequencies associated with a given cluster can be calculated [12-15]. For this purpose, we employed a normal mode procedure. After an energetically stable configuration for the cluster is found, the total potential energy is expanded about this minimum from which the force constants are determined [14,15]. A diagonalization of the force constant matrix produces the desired eigen frequencies. This procedure is for the  $T = 0^\circ\text{K}$  case and is based on the harmonic approximation.

For a system of three particles, eq. (6) may be put in a dimensionless form as:

$$\Phi^* = \sum_{i=1}^3 \sum_{j=1, j>i}^3 \left\{ \left( \frac{1}{r_{ij}^*} \right)^{12} - 2 \left( \frac{1}{r_{ij}^*} \right)^6 \right\} + Z^* \frac{1 + 3 \cos \theta_1 \cos \theta_2 \cos \theta_3}{(r_{12}^* \cdot r_{13}^* \cdot r_{23}^*)^3} \quad (7)$$

where the reduced quantities are defined by

$$\Phi^* = \frac{\Phi}{\epsilon} ; \quad Z^* = \frac{Z_1}{\epsilon r_0} \quad \text{and} \quad r_{ij}^* = \frac{r_{ij}}{r_0} .$$

Here, we also set  $m = 12$  and  $n = 6$  which reduces the two-body part of the potential to a Lennard-Jones function. This assumption simplifies the comparison of the present results with the earlier investigations [8,16-19] where the energetics and structural stabilities of clusters have been analyzed. The reduced potential energy,  $\Phi^*$ , when varied as a function of  $Z^*$ , produces either a linear or an equilateral triangular shape to be the energetically more stable form [8]. This is demonstrated in Fig. 1 for three different  $Z^*$ -values. In Fig. 1, the curves represent minimized total energies versus the angle  $\theta$  which was varied from  $50^\circ$  to  $180^\circ$  so as to include both configurations, equilateral triangle and linear. For  $Z^* = 0.2$ , no minimum is discernible for the linear case ( $\theta = 180^\circ$ ). For  $Z^* = 0.6$  and  $1.0$ , there are noticeable minima at  $\theta = 180^\circ$  which are more shallow than the equilateral triangular configuration ( $\theta = 60^\circ$ ). Other calculations [18-22] support this trend indicating that the energetically favorable structures would be either linear or "nearly" equilateral triangular.

Fundamental frequencies for the equilateral triangular and the linear configurations were estimated from corresponding characteristic equations based on the normal mode procedure. Each configuration exhibits a spectrum with frequencies  $\omega_1$ ,  $\omega_2$  and  $\omega_3$ . Figures 2a and 2b display calculated "reduced" frequencies  $\omega_i^*$  as functions of the three-body intensity parameter  $Z^*$ , for the triangular and linear cases, respectively. Reduced frequencies were calculated as  $\omega_i^* = \omega_i/\omega_0$  where  $\omega_0$  denotes the

corresponding diatomic normal mode frequency. For homonuclear cases, based on eq. (2), it is given by

$$\omega_0 = (2\pi m \epsilon / M)^{1/2} / r_0 \quad (8)$$

where  $M$  represents the atomic mass. For the linear configuration, the three main peaks corresponding to bending, symmetric and asymmetric vibrations were well separated. The bending mode exhibits the lowest frequency which is expected due to the shallow minimum at  $\theta = 180^\circ$  shown in Fig. 1. The peak corresponding to the asymmetric vibration, on the other hand, was found to be in the high frequency region. For the equilateral triangular case the asymmetric and bending modes become degenerate, as anticipated, and are located in a lower frequency region than the peak for the symmetrical vibration. These trends, for either configuration, remain unaltered for the range of  $Z^*$  (from 0.0 to 1.0) considered in this investigation. Calculated peak positions for the equilateral triangular configuration are consistent with results reported by Etters et al. [18] for the rare gas clusters. Their results represent a special case in our approach with  $Z^* = 0$ .

The effect of  $Z^*$  exerted on the peak positions for the linear and triangular configurations was found to be in opposite directions. For increasing three-body intensities, the two main vibrational peaks for the equilateral triangular shape shift to the lower frequency region, while the three peaks of the linear configuration shift to the higher frequency domain. The largest shift was found to be exhibited by the symmetric vibrational mode for the equilateral triangular case. Probably, the most

interesting region of  $Z^*$  values lies between 0.66 and 0.70 where the two configurations may coexist in appreciable concentrations. For  $Z^* = 0.68$  the equilateral triangular and linear shapes (with  $m = 12$  and  $n = 6$ ) become energetically degenerate. Accordingly, for systems with homonuclear triatomic clusters, one would anticipate a mixture of these species at roughly equal concentrations. Comparison of the calculated results with experiments for this special situation is difficult, not only because of the parametrical nature of the present study, but also because of various complications involved in the interpretation of the spectroscopic measurements. Recently, Richtmeier et al. [21] calculated vibrational frequencies for group IB trimers. For triangular configurations (not necessarily equilateral) they found that the symmetric stretch mode exhibited the highest frequency, while the bending and asymmetric vibrational frequencies were lower and relatively close to each other. Basically, these results are consistent with the present calculations based on the chosen parameters. Some effects due to different  $m$  and  $n$  values on the relative position of vibrational peaks are expected but they were not analyzed in this investigation.

## Conclusion

The calculated normal mode frequencies of homonuclear triatomic clusters were found to be affected considerably by the intensity of the three-body forces operational among the particles. For increasing intensity of the three-body forces, the two vibrational peaks for the equilateral triangular configuration shift to lower frequencies while the three peaks for the linear shape shift to the higher frequency domain. For homonuclear

triatomic clusters with  $Z^* = 0,68$ , the two species, i.e., the equilateral triangular and linear configurations, may coexist.

### Figure Captions

Fig. 1 Variation of the reduced potential energy,  $\Phi^*$ , as a function of  $\theta$  for three different  $Z^*$ -values.

Fig. 2 Reduced frequencies versus  $Z^*$ -values; (a) for the equilateral triangular configuration; (b) for the linear configuration.

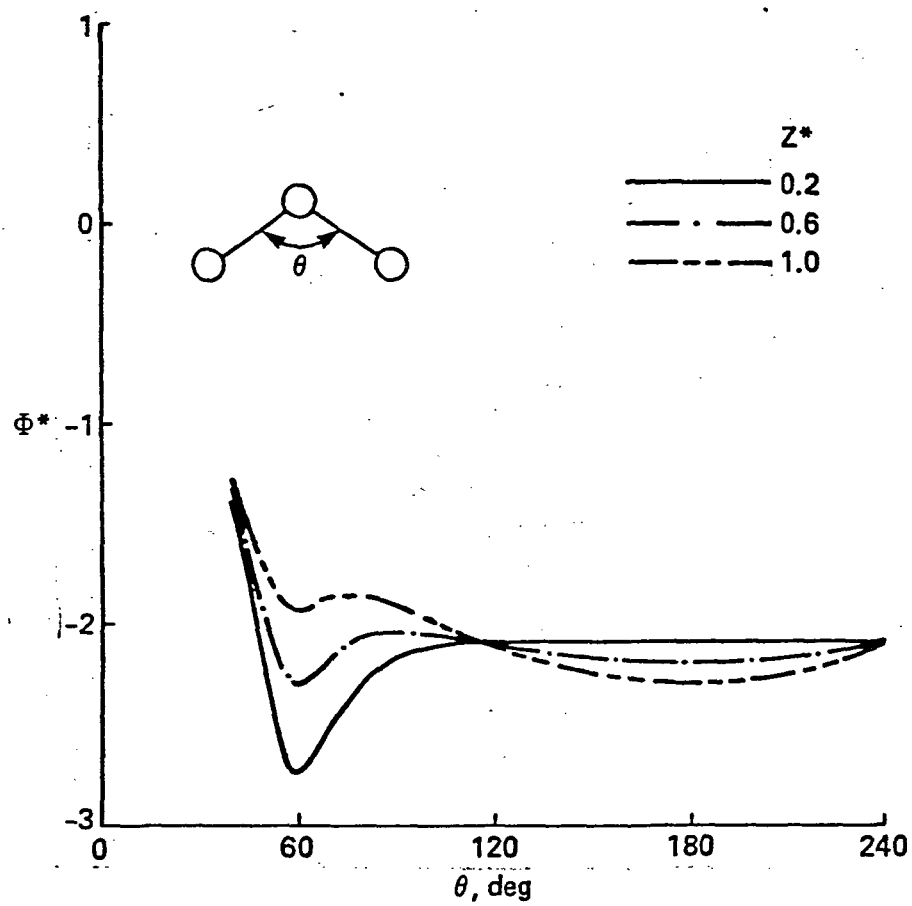


FIGURE 1

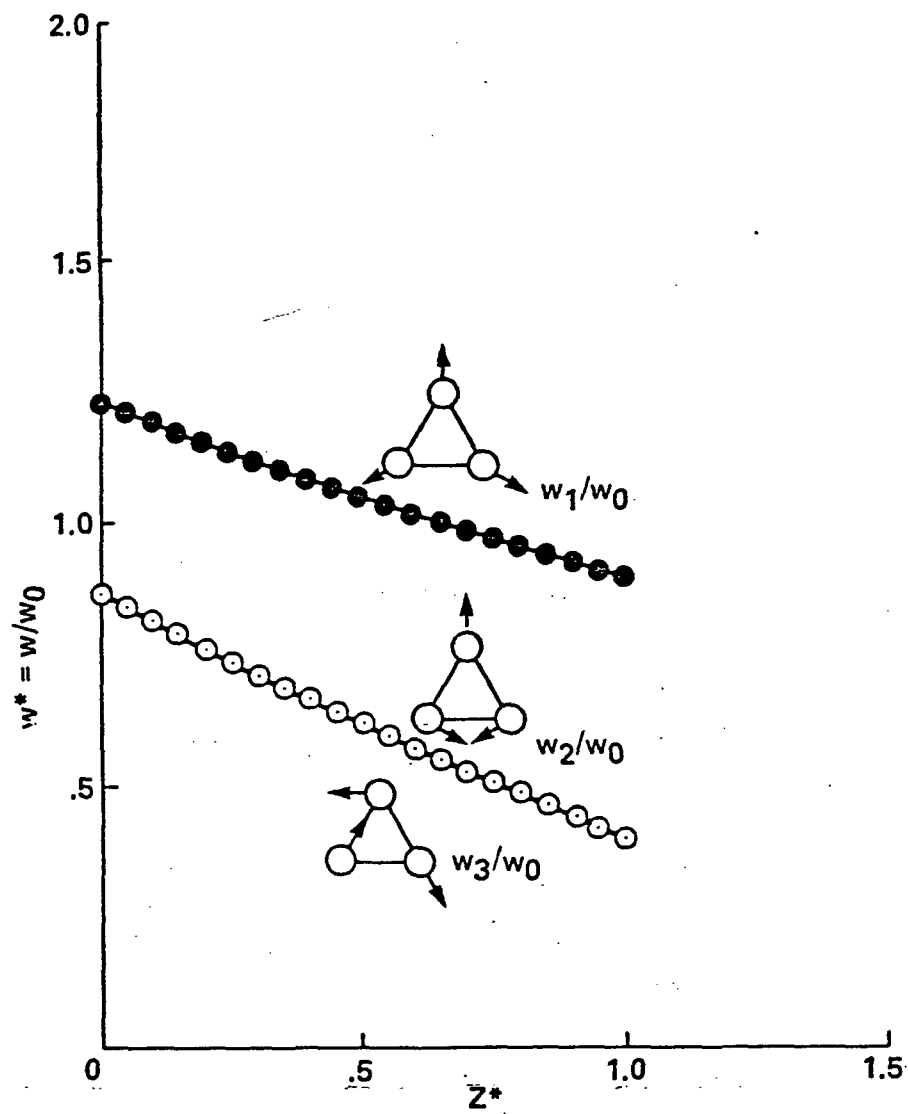


FIGURE 2(a)



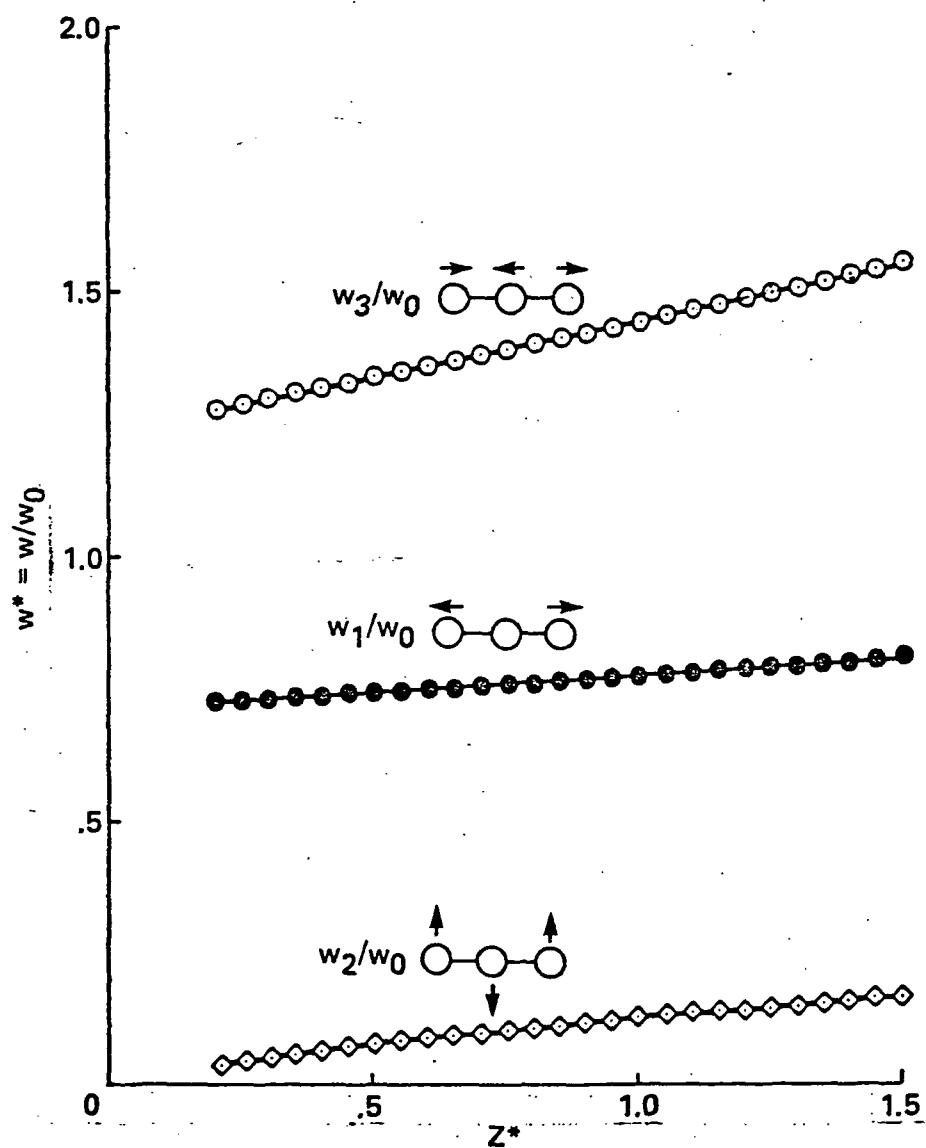


FIGURE 2(b)

## CHAPTER III

### Multilayer Relaxation Calculations for Low Index Planes of an FCC Crystal

In many studies related to surfaces the relaxation and the reconstruction of the exposed region are very important. Numerous experimental and theoretical works have been generated to explore and understand the atomic nature of the surface reconstruction phenomenon. Recent experimental findings indicate that in many metal surfaces a multilayer relaxation takes place. Surface region interlayer spacings differ from the bulk value considerably. In general, the most pronounced relaxation occurs in the spacing between the first and second atomic layers,  $d_{12}$ , which is found to be less than the corresponding bulk value [23-31]. These experimental results have been predicted first by Finnis and Heine [32] using a single layer relaxation approach. More recently Landman, Hill and Mostoller [33] calculated the reconstruction in metal surfaces using a multilayer relaxation procedure and obtained results consistent with experiments. In both of these approaches, calculations were performed employing surface electronic charge densities based on quantum mechanical considerations. Other theoretical calculations using only semi-empirical pair potentials, however, predict  $d_{12}$  to be larger than the bulk value which is in contradiction with experimental results. This shortcoming of the semi-empirical pair interaction models which are being used in many computer simulation calculations (because of their functional simplicity) inhibits their usage in various surface region modeling studies.

In this investigation, in order to improve the applicability of the semi-empirical potential models in calculations related to the surface structures, a potential energy function comprising two-body and three-body interactions was taken into consideration. As model systems (100), (110) and (111) index planes of an fcc crystal were employed. Three-body forces were found to be extremely important in the multilayer relaxation of these surfaces. The results of calculations showed a trend which was in good agreement with experimental findings.

Throughout this investigation the surface energy  $\sigma$  per atom was calculated from:

$$\sigma = \sum_{\ell}^M (e_{\ell} - e_0) \quad (9)$$

where  $e_{\ell}$  and  $e_0$  denote the total potential energy for an atom located in the  $\ell$ 'th surface layer (from the top) and of an atom located in the bulk of the system, respectively.  $M$  is the total number of the surface layers considered in the calculation.

The cut-off radius,  $R_{\text{cut}}$ , was taken to be approximately  $5r_0$ , in all cases. In the calculations of  $e_0$  (the energy per atom in the bulk) the stability condition for the crystal was taken into account by assuming:

$$\frac{\partial e_0}{\partial V} = 0 \quad (10)$$

with  $V$  denoting the total volume. For different  $Z$ , the values of  $e_0$  were calculated considering eq. (6) based on the condition imposed by

eq. (10). This approach has been employed in reference [5] in calculating stabilities of ideal crystals.

### Results and Discussions:

In numerical calculations, the units for the energy and distances were reduced by  $\epsilon$  and  $r_0$  (of eq. (2)), respectively. For the multilayer relaxation procedure the surface and bulk energies (i.e.,  $e_s$  and  $e_0$ ) were calculated for different  $Z$  values ranging from 0.0 to 0.4. Three different surface planes (100), (110) and (111) for an fcc crystal were included in the calculations. Relaxations were performed for the top-most five surface layers by minimizing the surface energy  $\sigma$  of eq. (9) with respect to the positions of the atomic layers. In this minimization procedure, for every  $Z$  value, the bulk energy  $e_0$  was calculated considering eqs. (6) and (10), simultaneously. The minimization involves a layer-by-layer relaxation which was carried out by varying the positions of the layers only in the perpendicular direction ( $z$ -direction). However, atomic arrangements within each layer (i.e.,  $x$ - $y$  planes) were left unaltered.

In Fig. 1, the energies calculated for three different surface structures and for the bulk were plotted versus the  $Z$  value. For all three cases, the surface energies were found to be monotonically decreasing functions of  $Z$ . The (111) surface has the lowest while the (110) exhibits the highest surface energy, as anticipated. On the other hand, the bulk energy  $e_0$  (the lowest curve) displays an opposite trend (i.e.,  $e_0$  increases with  $Z$ ). This curve reflects structural characteristics of an fcc crystal and depends only on the atomic configurations of the system [5].

Calculated results for the multilayer relaxation of (110), (100) and (111) index planes are shown in Figs. 2a, 2b and 2c, respectively, where percentage variations in the interlayer spacings  $d_{12}$ ,  $d_{23}$  and  $d_{34}$  were plotted versus  $Z$  values. The most dramatic relaxation took place for the (110) surface. For  $Z < 0.1$ , all three interlayer spacings of the (110) surface were found to be larger than the bulk value. On the other hand, for  $Z > 0.1$ ,  $d_{12}$  and  $d_{34}$  become progressively smaller than the bulk interlayer spacing, while the  $d_{23}$  continues to expand (see Fig. 2a). The  $d_{12}$  exhibits the largest variation among all. A relatively smaller relaxation took place for the (100) surface. Up to  $Z \approx 0.2$  all three interlayer spacings remain larger than the corresponding bulk value. For  $Z > 0.2$ , the  $d_{12}$  exhibits some contraction, while the variations in the  $d_{23}$  and  $d_{34}$  with respect to the bulk value remain negligibly small (see Fig. 2b). For the (111) surface, we found the smallest relaxation; however, the variation in the  $d_{12}$  still displays a similar trend as in (110) and (100) cases. Up to  $Z \approx 0.3$ , again all three interlayer spacings were found to be somewhat larger than the bulk value. In this case, percentage variations in  $d_{23}$  and  $d_{34}$  for  $z > 0.3$  are negligible. Only the  $d_{12}$  exhibits a small contraction for  $Z$  values larger than 0.3 (see Fig. 2c).

The quantity  $\theta$  which is defined as  $|\sigma/e|$  is a useful property and can be regarded as the "relative" surface energy [36]. Figure 3 shows the values of  $\theta$  plotted versus  $Z$  for (110), (100) and (111) surface planes. The overall trend is similar to the variation of  $\sigma$  in Fig. 1. The (111) plane remains as the energetically most favorable surface, consistently; and (110) is the least stable one bearing the highest surface energy. Values of  $\theta$  calculated for  $Z = 0$  (which is a special case in our

approach) are in good agreement with results reported by Benson and Claxton [36].

Results obtained in this multilayer relaxation calculation (for the low index planes of fcc crystals) are in good qualitative agreement with recent experimental findings [23-31]. For the  $Z = 0.3$  case, the calculated percentage variations in  $d_{12}$ ,  $d_{13}$  and  $d_{34}$  for the (110) plane were found to be -9.98, +5.52 and -1.81, respectively; and, for the (100) plane, -1.63, -0.00 and +0.02, respectively. For comparison, Davis and Noonan [23] using a LEED technique obtained  $\Delta d_{12} = -10.0 \pm 2.5\%$  and  $\Delta d_{23} = 0.0 \pm 2.5\%$  for the (110) surface; and  $\Delta d_{12} = -1.1 \pm 0.4\%$  and  $\Delta d_{23} = +1.7 \pm 0.6\%$  for the (100) plane of copper. In another study based on a High Energy Ion Scattering experiment, I. Stensgaard et al. [27] obtained  $\Delta d_{12} = -5.3 \pm 1.6\%$  and  $\Delta d_{23} = +3.3 \pm 1.6\%$  for the Cu (110) surface. Furthermore, studies of the Cu (110) surface, which have been carried out by Adams et al. [30] based on LEED measurements, produced  $\Delta d_{12} = -8.5\%$  and  $\Delta d_{23} = 2.3\%$ . In general, we found a very small surface relaxation for the (111) plane. This conclusion is well supported by various experimental reports on the (111) surfaces [29,27]. Another comparison with experiments is possible for the surface energy of copper. The experimental value of  $\theta$  (surface energy per atom/absolute cohesive energy per atom) is 0.172 [37]. Our multilayer relaxation calculations for  $Z = 0.3$  produced  $\theta = 0.185$  which can be considered in fair agreement with the above results for the (111) surface plane.

These comparisons indicate that, for the present potential energy function, the best  $Z$ -value for Cu should be around 0.3. Calculated results also agree with the more recent experimental work by Andersen et

al. [29] for the multilayer relaxation of Al (110) surface. Furthermore, our calculations support the multilayer relaxation results obtained by Landman et al. using an electronic charge density method based on more accurate quantum mechanical considerations. There, they also reached the same conclusion: that the central two-body potentials alone are not sufficient to describe the surface region properly [33,34].

However, care must be exercised in comparing these calculated multilayer relaxation results with experimental findings. The calculations of the  $d_{ij}$ 's and of  $\theta$  require only the knowledge of  $m$ ,  $n$  and  $Z$  parameters. If the absolute values of  $e_\lambda$ ,  $e_0$  and  $d_{ij}$  are desired,  $\epsilon$  and  $r_0$  are also needed. All these potential energy parameters must be determined from the physical properties of the materials under consideration.

The relationship between these potential energy parameters and the crystal structure has been shown elsewhere [5]. The stability region of a crystal structure depends on the values of  $m$  and  $n$  as well as  $Z$ . In the present investigation we analyzed the dependence of the multilayer relaxation on the value of  $Z$ , the three-body intensity parameter. However, we believe that an analysis of the effect of  $m$  and  $n$  values (of the two-body potential) would be an interesting study.

## Conclusions

The most significant outcome of the present investigation is the understanding of the important effect exerted by the many-body forces on the multilayer relaxations of surfaces. Consideration of the three-body interactions corrects the shortcomings of pair potential models, and furnishes relaxed surface configurations with varying interlayer spacings which agree (at least qualitatively) with various experimental measurements.

For the low index surface planes of an fcc crystal, the importance of the multilayer relaxation increases as  $(111) \rightarrow (100) \rightarrow (110)$ ; i.e., with decreasing atomic density of the plane. The first interlayer spacing  $d_{12}$  is found to be increasing for smaller three-body interaction intensities ( $Z$ ), but decreasing for systems with higher  $Z$ . The second layer spacing  $d_{23}$  tends to increase monotonically with increasing  $Z$  on the  $(110)$  surface, but decreases slightly on the other two surfaces. The percentage variation in the  $d_{34}$  is generally negligible, except for the  $(110)$  case where it is noticeable and decreases with  $Z$ .

The potential energy employed in this study has a relatively simple functional form; therefore, it may be used in lengthy computer simulation calculations related to surfaces.



## Figure Captions

Fig. 1 Change in energy per atom versus  $Z$  for different surfaces and at bulk. Both quantities, energy and  $Z$ , are in reduced units.

Fig. 2 Percentage change in interlayer spacings for different surfaces as a function of  $Z$ . Thick solid line, thin solid line, and dashed line represent percentage changes in  $d_{12}$ ,  $d_{23}$ , and  $d_{34}$  respectively.

Fig. 3 Ratio of the energy per atom at the surface to the absolute bulk value,  $\theta$ , for different surface planes as a function of  $Z$ .

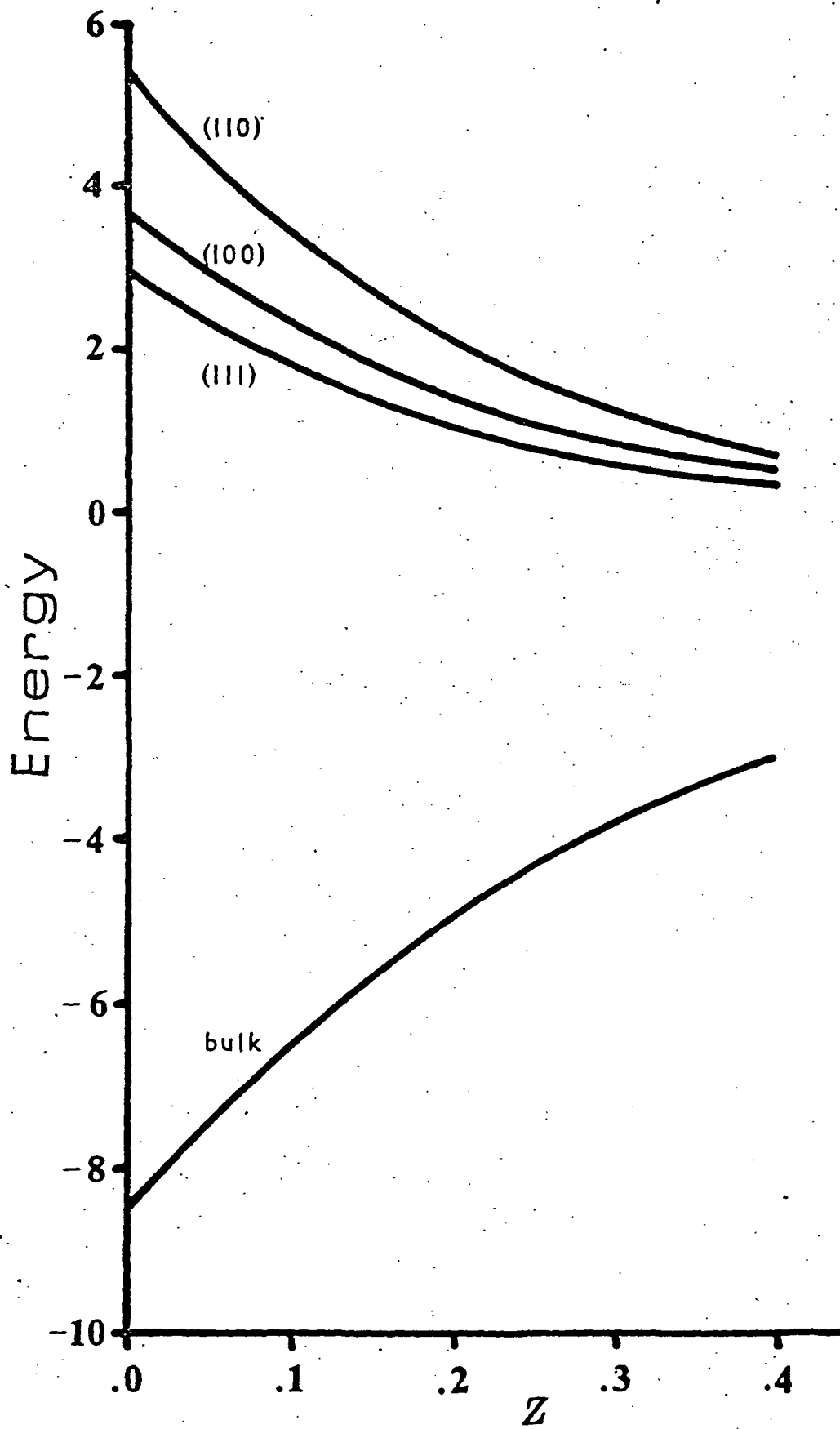


FIGURE 1

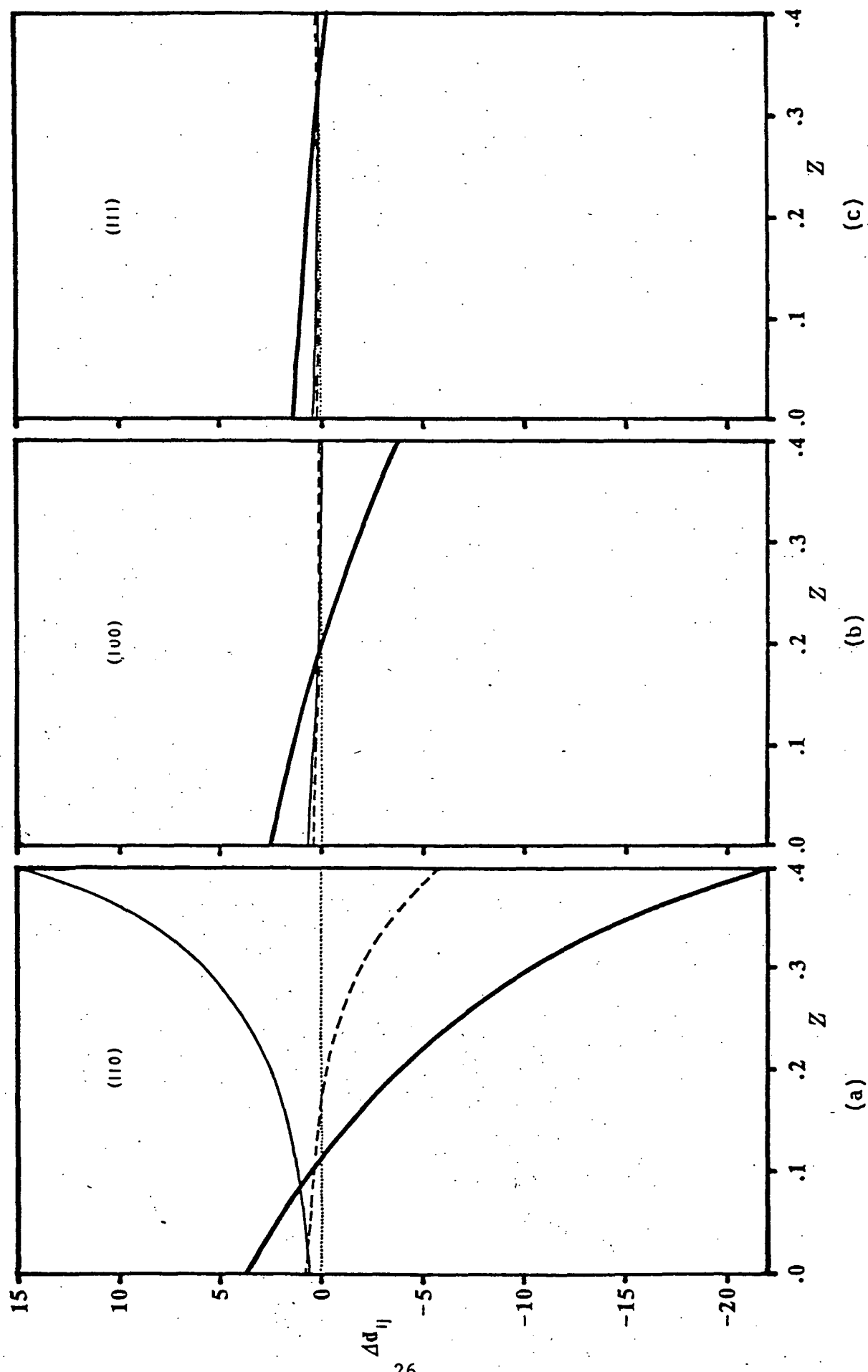


Figure - 2

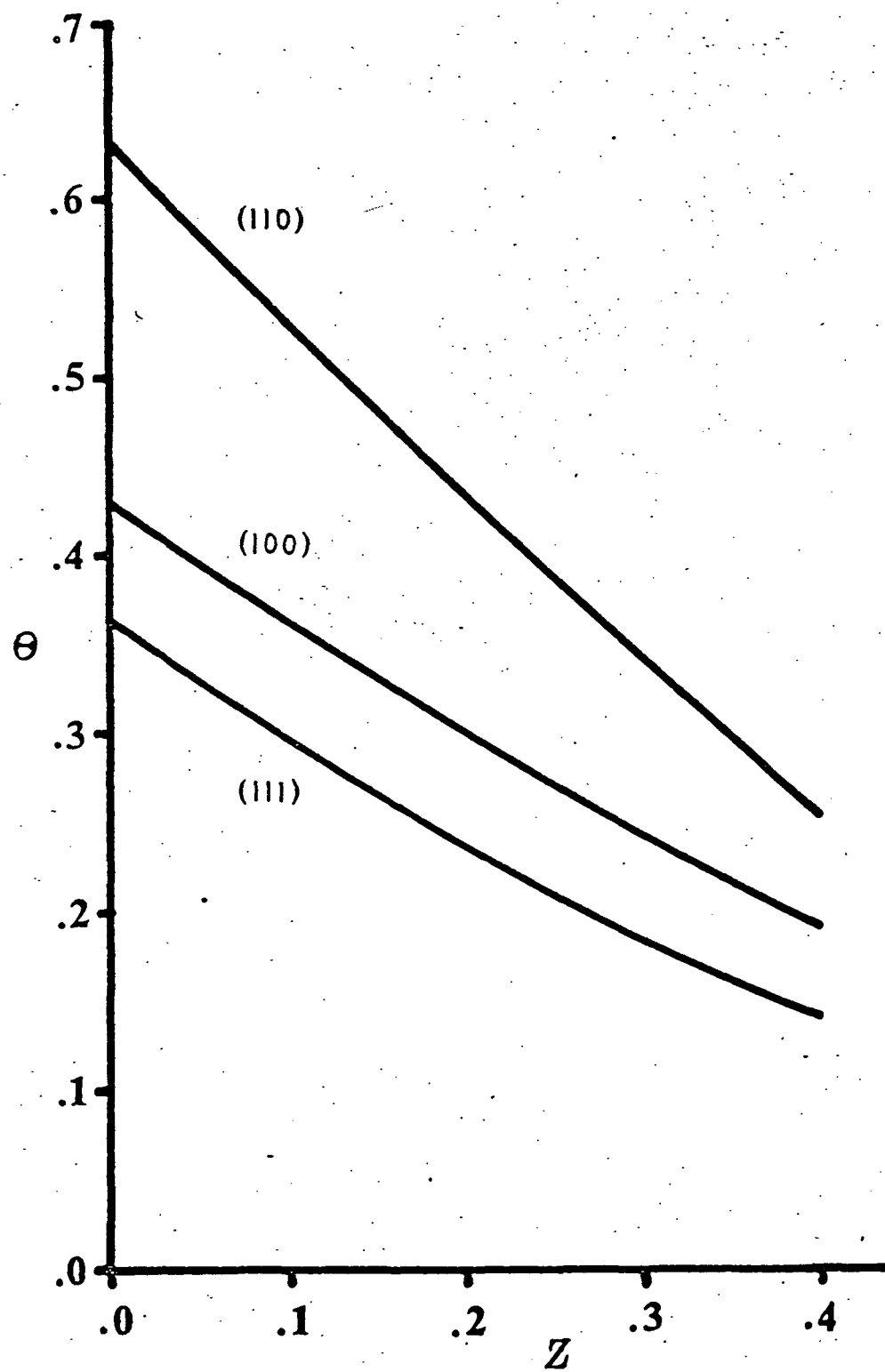


FIGURE 3

## CHAPTER IV

### Evaluation of Parameters

In order to calculate the total potential energy for a system of  $N$  particles in a given configuration, the parameters ( $\epsilon$ ,  $r_0$ ,  $m$ ,  $n$  and  $Z$ ) of eqs. (2)-(5) must be known. By definition, these parameters are materials constants and depend on the atomic species involved in the interaction. For a crystalline system the total potential energy expressed by eq. (6) may be simplified employing Lattice sum representations:

$$\Phi = \frac{N}{2!} \frac{\epsilon}{m-n} \left[ n \left( \frac{r_0}{d} \right)^m A_m - m \left( \frac{r_0}{d} \right)^n A_n \right] + \frac{NZ}{d^9} T_k \quad (11)$$

where  $d$  is the nearest neighbor distance in the crystal. The lattice sum  $A$ 's and  $T_k$  are given by

$$A_\lambda = \sum_i \left( \frac{d}{r_i} \right)^\lambda \quad (12)$$

and

$$T_k = \frac{1}{3!} \sum_{\substack{j, k \\ j \neq k}} \frac{(1 + 3 \cos \theta_i \cdot \cos \theta_j \cdot \cos \theta_k)}{\left( \frac{r_{ij}}{d} \right)^3 \left( \frac{r_{ik}}{d} \right)^3 \left( \frac{r_{jk}}{d} \right)^3} \quad (13)$$

These lattice sums are simply geometrical factors and only depend on the crystal structure [5,7]. Table 1 tabulates calculated values of  $A_\lambda$  for different  $\lambda$ , along with the  $T_k$  values for various crystal

geometries. In the evaluation of parameters we also used the stability criterion which is given by:

$$\left(\frac{\partial \Phi}{\partial V}\right)_T = 0 \quad (14)$$

where  $V$  denotes the total volume of the system. This relation is exact only at  $T = 0^\circ\text{K}$ . However, it has been always assumed that at relatively lower temperatures the minimum of the  $\Phi$  with respect to  $V$  coincides with the minimum of the free energy. Furthermore, the second derivative of the energy is related to the bulk modulus by:

$$B = V \left( \frac{\partial^2 \Phi}{\partial V^2} \right)_T \quad (15)$$

For simplicity as well as for proper comparison of the results with other Lennard-Jones calculations, in this project, generally, we considered that the exponents in the two-body potential function are  $m = 12$  and  $n = 6$ . Now, with this assumption, the remaining three unknown parameters can be calculated from eqs. (11) through (15), using experimental cohesive energy and the bulk modulus. However, in some cases, these non-linear simultaneous equations cannot be solved. Therefore, for those cases, we used either surface energy values or experimental small cluster data for the fitting procedure.

Table 1

Lattice Sums of the Mie Potential and the Axilrod-Teller Potential for Various Structures (One Component System)

	HCP	FCC	BCC	SC	DIA	GRAH
A <sub>4</sub>	23.616	25.5946	21.1685	15.485	9.5795	5.4351
A <sub>5</sub>	16.883	16.8807	14.6913	10.333	6.2862	3.8825
A <sub>6</sub>	14.449	14.4481	12.2495	8.3994	5.1153	3.3895
A <sub>7</sub>	13.360	13.3590	11.0539	7.4669	4.5944	3.1910
A <sub>8</sub>	12.803	12.8019	10.3551	6.9458	4.3310	3.0993
A <sub>9</sub>	12.493	12.4926	9.8945	6.6289	4.1904	3.0534
A <sub>10</sub>	12.312	12.3113	9.5644	6.4261	4.1110	3.0294
A <sub>11</sub>	12.201	12.2009	9.3132	6.2923	4.0655	3.0164
A <sub>12</sub>	12.132	12.1319	9.1141	6.2021	4.0389	3.0092
A <sub>13</sub>	12.088	12.0877	8.9518	6.1406	4.0233	3.0052
A <sub>14</sub>	12.059	12.0590	8.8167	6.0982	4.0140	3.0030
A <sub>15</sub>	12.040	12.0400	8.7030	6.0688	4.0086	3.0017
A <sub>16</sub>	12.027	12.0274	8.6063	6.0483	4.0051	3.0010
A <sub>17</sub>	12.019	12.0198	8.5236	6.0339	4.0031	3.0005
A <sub>18</sub>	12.013	12.0130	8.4525	6.0239	4.0019	3.0003
A <sub>19</sub>	12.009	12.0094	8.3914	6.0168	4.0011	3.0002
A <sub>20</sub>	12.006	12.0063	8.3386	6.0119	4.0007	3.0001
T <sub>k</sub>	19.175	19.1697	14.7719	6.6138	1.6647	0.1010
#†	7200	6912	8192	8000	5832	5040

† Indicates the number of atoms which were considered to compute the lattice sums.

For covalent materials such as Si, C and SiC we calculated the parameters using eqs. (11) and (14), plus the small cluster data. The calculated results are given in Table 2. In the rest of this report, those parameters will be employed in various simulation calculations.

Table 2

Constant Set in the Two- and Three-body Parts  
for Si, C and SiC

---

$m(\text{Si}, \text{Si}) = 12$	$n(\text{Si}, \text{Si}) = 6$	$\epsilon_{\text{Si}, \text{Si}} = 3.228(\text{eV})$	$R_0^{\text{Si}, \text{Si}} = 2.29505(\text{\AA})$
$m(\text{Si}, \text{C}) = 12$	$n(\text{Si}, \text{C}) = 6$	$\epsilon_{\text{Si}, \text{C}} = 4.462(\text{eV})$	$r_0^{\text{Si}, \text{C}} = 1.74(\text{\AA})$
$m(\text{C}, \text{C}) = 12$	$n(\text{C}, \text{C}) = 6$	$\epsilon_{\text{C}, \text{C}} = 6.2295(\text{eV})$	$r_0^{\text{C}, \text{C}} = 1.4806(\text{\AA})$
$Z_{\text{Si}, \text{Si}, \text{Si}} = 3991.7(\text{eV} \cdot \text{\AA}^9)$		$Z_{\text{Si}, \text{Si}, \text{C}} = 800.0(\text{eV} \cdot \text{\AA}^9)$	
$Z_{\text{Si}, \text{C}, \text{C}} = 300.0(\text{eV} \cdot \text{\AA}^9)$		$Z_{\text{C}, \text{C}, \text{C}} = 191.73(\text{eV} \cdot \text{\AA}^9)$	

---

To investigate the applicability of these calculated parameters, several tests were carried out.

Under normal conditions, silicon has a diamond cubic structure. Under high pressures, however, it undergoes to a phase transformation. The high pressure form of silicon has a tetragonal  $\beta$ -tin structure. This structural transformation is accompanied by a large volume decrease ( $\sim 22.7\%$ ). First, a simulation calculation was performed to analyze this phase transformation phenomena. For silicon we considered four different crystalline structures (including diamond cubic,  $\beta$ -tin, fcc and bcc) and using the same set of parameters we calculated the total energy as a function of the total volume. This is shown in Fig. 1 which clearly indicates the energetically most favorable structure is the diamond cubic. Under higher pressures (i.e., for smaller volumes), the  $\beta$ -tin structure becomes energetically



more stable. According to this calculation, other structures may become stable at much higher pressures. The calculated change in volume for the transformation is in good agreement with the experimental data.

Next, the melting process of silicon was simulated using again the same set of parameters. A constant pressure Monte-Carlo calculation was employed to simulate a silicon system which contained 64 atoms with periodic boundary conditions in all three directions. For every incremental temperature step (from 300°-5000°K), the system was equilibrated which was monitored by the variation of the total energy. In Fig. 2, the total energy, relative volume and the bulk modulus values are plotted as a function of the temperature. All three of these functions exhibit changes of slope around  $T = 2000^{\circ}\text{K}$ . Furthermore, calculated radial distribution functions as well as trajectory plots of the particles indicate that the melting takes place at  $\sim 2000^{\circ}\text{K}$ . This is somewhat higher than the experimental melting point of silicon, however, the ability for the potential energy function to provide a proper volume decrease during the melting process was considered as an important accomplishment.

Further checks for the adequacy of the parameter set involved also the investigation with pure carbon. The potential energy function for C with parameters tabulated in Table 1 can provide two closely spaced energy levels for diamond and graphite. Calculated energies are somewhat larger than the experimental values; however, the calculation predicts that the lower lying state belongs to graphite. Also, for the case of SiC the potential energy provides two almost degenerate energy states corresponding to  $\alpha$  and  $\beta$  forms of SiC, consistent with experimental data.

## Figure Captions

Fig. 1 Total energy curves for the four structures of Si as a function of the atomic volume. Dashed line is the common tangent of the energy curves for the diamond cubic and  $\beta$ -tin structure ( $c/a = 0.546$ ).

Fig. 2 (a) The total energy, (b) the volume and (c) the bulk modulus of the system as a function of temperature at the equilibrium state.

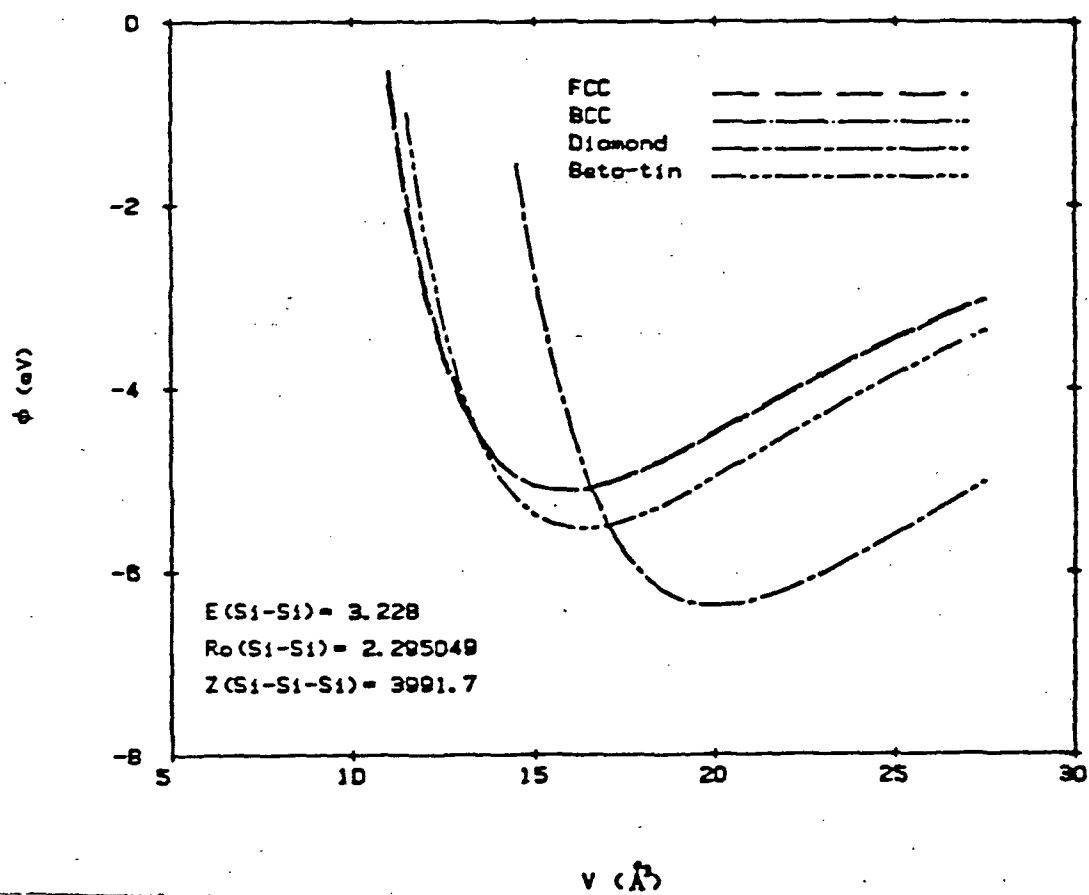


FIGURE 1

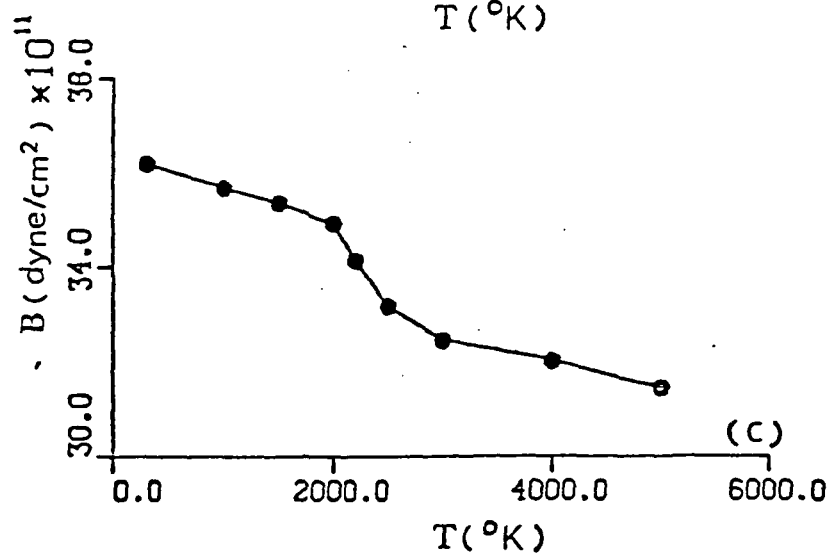
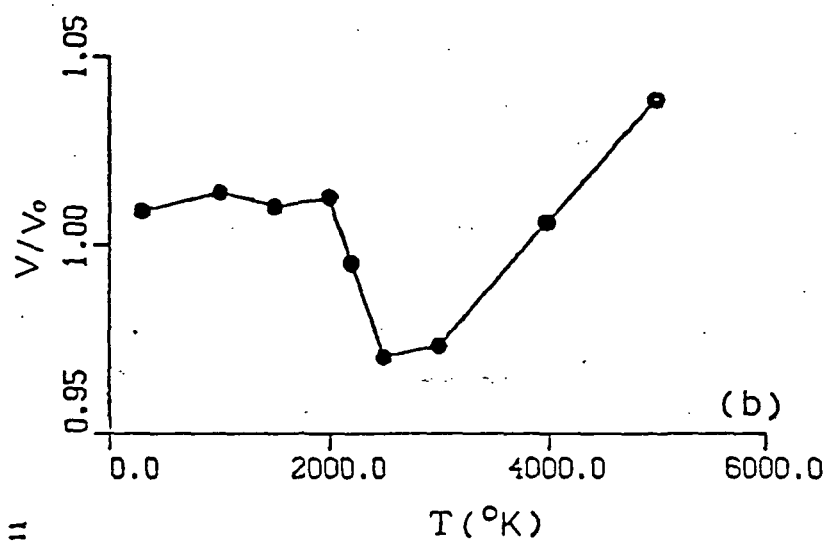
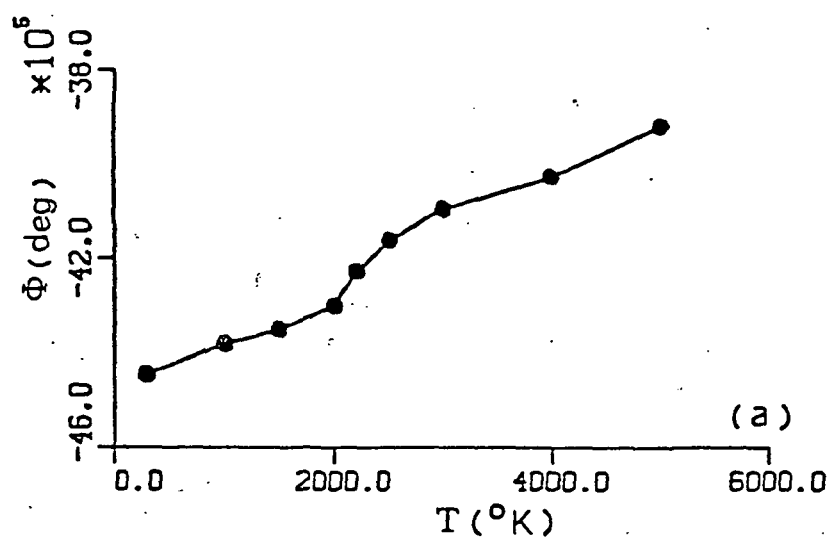


FIGURE 2

## CHAPTER V

### Simulation for Surface Properties

Detailed atomistic level information about clean solid surfaces is very important in the analysis of various surface processes. Calculation of surface properties from interatomic potentials is an involved procedure due to the fact that the role played by many-body forces at the surface region is not negligible. For an accurate simulation calculation these many-body effects must be accounted for properly [35]. In particular, for substances like Si or SiC which were considered in this investigation, the many-body interactions are shown to be very significant.

Surfaces were generated in the computer as abrupt discontinuities of the crystalline bulk. To obtain relaxed (or reconstructed) surfaces, this initial configuration was permitted to relax under the Monte-Carlo code.

In general, we applied periodic boundary conditions in two-directions which provided an effectively infinite exposed surface in the desired direction. Relaxation procedures were carried out for the top three to five atomic layers (depending on the surface geometry). The rest of the atoms in the system were fixed in their original lattice sites. However, the fixed atoms contributed fully to the total energy calculation.

#### Si(100) Surface:

Calculations for Si(100) surface were performed at two different temperatures employing a Monte-Carlo procedure. At  $T = 298^\circ\text{K}$  the equilibrated structure of Si(100) exhibited a  $c(2 \times 2)$  reconstruction. As it is shown in Fig. 1, the atoms at the top layer tend to form pairs. This

feature is quite similar to reconstructed models of Si(100) suggested by various investigators [38-41]. It is now accepted that the general tendency in the structural reconstruction of the Si(100) surface is the formation of dimers as originally suggested by Schlier and Farmworth [42]. More than one type of reconstruction patterns may coexist on Si(100) surface (e.g., not only  $(2 \times 1)$ , but possibly  $c(4 \times 2)$ ,  $p(2 \times 2)$  and  $c(2 \times 2)$  superstructures as well). Our result  $c(2 \times 2)$  represents one of these reconstruction models.

Atoms located in the second and third layers remained more or less stationary. Interplanar spacings between the first and the second layers displayed a contraction, while other interlayer spacings were affected only marginally. Our calculated results for the interplanar relaxation are quite consistent with results reported by Yin and Cohen [43] who employed an ab initio self-consistent pseudopotential method.

The surface energy calculated from an equilibrated Si(100) surface was found to be  $1386 \text{ ergs/cm}^2$  which is in good agreement with experimental data [37]. At low temperatures ( $T \approx 1^\circ\text{K}$ ) on the other hand, it was found that the surface structure after relaxation preserved its  $(1 \times 1)$  symmetry (i.e., no dimer formation was observed). However, the first interlayer spacing for the equilibrated Si(100) surface exhibited a contraction as in the previous case explained above.

In the second part of this chapter, statics calculations were performed for the stress tensor components as well as the energetics and the structure for the (111) surfaces of Si and SiC.

The major contribution to the stresses in a system of interacting particles is the strain derivative of the potential energy. Since the PEF

used is a sum of terms depending on only a few atoms at a time, the stress is also. It is thus possible to define a potential and stress for each atom in units of energy/atom. In the next section, these atomic quantities are plotted using the corresponding atomic positions to present a qualitative description of the highly non-homogeneous behavior of the surface or defect.

A variety of excess energies and formation energies are reported in the following section. They have been calculated using the general expression:

$$E_{\alpha}^{\text{ex}} = \frac{1}{C_{\alpha}} (E_T - N_T \phi - \sum_{\beta} C_{\beta} E_{\beta}^{\text{ex}}) . \quad (16)$$

$E_T$  is the total energy for the simulation of  $N_T$  atoms with bulk energy per atom  $\phi$ .  $C$  is a normalization factor, such as area or length. The final term in eq. (16) subtracts all other appropriate total excess energies. Thus, for example, the ledge excess,  $\lambda$ , would be:

$$\lambda = \frac{1}{L_T} (E_T - N_T \phi - A_T \gamma) \quad (17)$$

where  $\gamma$  is the flat surface excess energy determined by a previous simulation,  $A_T$  is the total exposed surface area in the simulation with a ledge crossing it of total length  $L_T$ . Of course, these excess energies are not free energies, but internal energies. All of the results of the next section are thus subject to modified interpretations depending on the possible entropic effects for the "real" system.

## Silicon (111) Surface Properties:

### 1) Perfect Surface

When the diamond cubic lattice is terminated on a (111) plane, the unrelaxed geometry is as shown in Fig. 2(a) and 2(b). The pairs of layers (C-a), (A-b), or (B-c) are best considered as one "puckered" layer of "upper" and "lower" atoms, designated by open and filled circles respectively. The intra- and inter-layer spacings for the bulk are  $\delta = .7839$  and  $\Delta = 2.3516 \text{ \AA}$ . The region enclosed by dashed lines in Fig. 2(b) is the primitive two-dimensional surface unit cell.

If we take these perfect crystal positions as the initial positions, then our relaxation calculations show a 27% contraction of the outermost layer to  $\delta_1 = 0.574$ , and a slight expansion of the other distances  $\Delta_1$ ,  $\delta_2$ ,  $\Delta_2$ ; by 1.6, 1.4, and 0.05 percent respectively. The layers remain flat and otherwise unreconstructed. Our calculation relaxed four puckered layers of 50 atoms each ( $A_T = 319.25 \text{ \AA}^2$ ) to a final total energy of -1230.50 eV, yielding  $\gamma = 1169 \text{ ergs/cm}^2$ . Figure 2(c) shows the potential energy distribution in the first four surface layers. Although the surface energy is positive as it must be, notice that the potential energy of the "lower" atoms in the first layer is actually more negative (more strongly bonded) than atoms in the bulk due to the surface reconstruction.

Figure 2(d) shows the stress,  $\tau_{11}$ , for the first four surface layers.  $\tau_{11}$  is the normal stress along the  $(01\bar{1})$  direction (in the plane of the surface), and was found to be identical to the normal stress along the  $(\bar{2}11)$  direction. The surface is evidently in compression relative to the bulk. If the total stress in the first two layers is assumed to be distributed over the region indicated in the figure, we can convert eV/atom to



energy/volume, with the result that  $\bar{\tau}_{11} = 61437$  atm. We can draw two immediate conclusions: (i) if the crystal is expanded for any reason (thermal strain, substrate misfit, etc.), the surface excess energy will decrease, and (ii) defects which generate local tensile fields will be attracted to the surface.

## 2) Perfect Ledges:

There are two unequivalent high-density ledges which terminate terrace layers on the (111) surface: the  $(\bar{2}11)$  and  $(2\bar{1}\bar{1})$ . If we consider Fig. 1(b) as a terrace, then these ledges are to the left and right respectively. The dashed lines indicate the "broken bonds" along the ledge. We have simulated both of these ledges separately. The periodic boundary conditions were established such that the ledges were widely spaced at 26.6 Å (8 surface unit cells). After relaxation, the ledge excess energies were found to be  $\lambda_{(\bar{2}11)} = 0.30$  eV/Å and  $\lambda_{(2\bar{1}\bar{1})} = 0.16$  eV/Å.

One might initially expect that the  $(\bar{2}11)$  ledge would have a lower ledge excess energy due to the fewer number of "broken bonds." However, the  $(2\bar{1}\bar{1})$  ledge undergoes a major reconstruction, in which alternative pairs of ledge atoms form dimers as shown in Fig. 3(a), with a spacing of 2.33 Å. It is this reconstruction which causes the  $(2\bar{1}\bar{1})$  ledge to be energetically favored over the  $(\bar{2}11)$ . This result agrees qualitatively with other theoretical calculations [44] and with cleavage experiments [45].

The energy and stress distributions around the lower energy ( $2\bar{1}\bar{1}$ ) ledge are shown in Fig. 3(c)-(e). The plots are of the quantities in eV/atom for all the atoms on one (111) layer; starting from the right of Fig. 3(b) at a ledge, moving left across the terrace, moving under the next ledge, etc. There is a one-to-one correspondence between the positions of the atoms in the indicated layer in Fig. 3(b) and the positions of the peaks in the plots below it.

The potential energy distribution, Fig. 3(c), shows only a small transition region as the layer passes under the ledges. The values for the energy per atom halfway between the ledges agrees to within 0.3% with the values from Fig. 2(c) for the perfect surface. From this, we might conclude that the ledges are not interacting at this spacing. However, consider Fig. 3(d), the normal stress directed parallel to the ledge,  $\tau_{zz}$ . The dotted line indicates the value for the larger peak from Fig. 2(d). The ledges are thus interacting even at this large spacing, since the stress does not achieve the perfect surface value. The ledges act to decrease the compressive character of the upper surface in the ledge-parallel direction; however, the overall effect is not as simply characterized. The most distinctive effect due to the ledge is the development of the shear stress field,  $\tau_{xy}$ , surrounding it, as seen in Fig. 3(e).

Several features should be emphasized. First, the reconstruction of the ledge opens up large holes along it which may become favorable sites for impurity adsorption. Second, the stresses, and in particular the shear stress, indicate how the ledge may affect other defects in the system.

### 3) Kink Site:

Investigation of the behavior of kink sites on the  $(2\bar{1}\bar{1})$  ledge has just begun. The kink site excess energy is 1.67 eV and it has only a minor effect on the stress distributions around the ledge. It is important to note that the "motion" of the kink site requires the addition of four atoms, due to the dimer reconstruction of the ledge. The activation energy for Si adatom attachment at the kink site will be strongly influenced by this fact.

### 4) Adatoms and Surface Vacancies:

The two most likely adsorption sites for single Si adatoms on the otherwise flat (111) surface are the three-fold coordinated sites [46]. The "cradle" site has a "lower" atom directly underneath it while the "hole" site does not (see Fig. 4). The surface vacancy is created by removing one "upper" atom. The defect formation energy  $E_f$ , as calculated by eq. (16), can be considered as the energy change in the system using a kink site (i.e., the bulk potential energy per atom) as a source or sink of atoms, and is a measure of the stability of the surface to the formation of these point defects.

The formation energies were determined for an effective surface defect concentration of 2% (1 defect every 25 surface cells). The cradle, hole, and vacancy energies are, respectively, 0.84, -0.31, and -1.19 eV. The perfect surface thus lowers its energy by 1.50 eV in creating a hole/vacancy pair, and no adjacent ledge is required as a source or sink of atoms. A further calculation showed a reduction to  $E_f = -1.82$  eV if the hole and vacancy associate on adjacent surface sites (surface Frenkel

pair). Our potential thus predicts that the (111) surface will spontaneously roughen, or reconstruct, to some equilibrium geometry of adatoms and vacancies. This behavior provides a basis for the interpretation of the  $(7 \times 7)$  reconstruction pattern observed on the Si (111) surface by LEED and STM experiments [46-48]. Further analysis of this effect is in progress.

The surprising stability of the surface vacancy depends on two effects. First, the vacancy generates tensile fields in the surrounding lattice and is thus favored in the highly compressive region at the surface. Even for the small concentration of defects used above, there was an 85% reduction in the surface compression (relative to the flat surface) for the vacancy, as compared to only a 6% increase in the surface compression for a hold adatom. The second effect is a strong reconstruction around the vacancy as shown in Fig. 3. The lower atoms surrounding the vacant site pull together in a configuration similar to the dimer reconstruction on the  $(2\bar{1}\bar{1})$  ledge. If we prohibit this reconstruction, the vacancy formation energy becomes +2.68 eV, which is consistent with other calculations for the unreconstructed surface vacancy energy [49].

## B) Silicon Carbide (111) Surface Properties

Many of the calculations described above have also been performed for the equivalent geometries on the (111) faces of SiC in the zincblend structure. We will briefly summarize the results obtained.

The zincblend binary structure has two unequivalent (111) faces, which in this case can be referred to as C-rich and Si-rich. The latter undergoes only a 5% contraction of the first layer, leading to  $\gamma = 2544 \text{ ergs/cm}^2$

and  $\bar{\tau}_n = 20170$  atm. The C-rich face, however, develops an outer layer contraction of 35% leading to  $\gamma = 344$  ergs/cm<sup>2</sup> and  $\bar{\tau} = -100619$  atm. The crystal growth properties of these two surfaces should thus be quite different. This places enormous importance upon the initial nucleation even for the SiC since a given heterogeneous substrate may favor one orientation over the other.

Since the C-rich face is so much more stable, we have concentrated on it. The  $(\bar{2}11)$  and  $(2\bar{1}\bar{1})$  ledges on this face have excess energies of 0.50 and 0.96 eV/Å respectively. Analysis of the geometry of the  $(2\bar{1}\bar{1})$  ledge shows that the dimer reconstruction is very minor compared to the silicon case, thus the  $(\bar{2}11)$  ledge is more stable as expected from the simple broken-bond argument. The stress distributions around the  $(\bar{2}11)$  ledge are similar to the silicon  $(2\bar{1}\bar{1})$  ledge as in Fig. 3(c-e), except that the sign of the shear stress is reversed at all points.

The formation energy for carbon and silicon adatoms in the hole sites on the C-rich face are -6.11 and +2.66 eV respectively, based upon the individual bulk energies per atom in the SiC crystal of  $\phi_{Si} = -9.995$  eV and  $\phi_C = -7.6627$  eV. The individual formation energies are somewhat arbitrary, but they do indicate that the carbon is much more strongly adsorbed onto the surface than the Si. The "smaller" carbon adatom is drawn down almost to the same level as the other C atoms on the surface, while the Si adatom remains approximately 1.3Å above the surface.

Very useful qualitative insights concerning surface energetics and surface processes can be gained from computer simulation studies using two-body plus three-body PEF's. The behavior of the stress distributions around these same structural elements has been described. This is an

especially useful tool for describing and predicting the overall growth process in terms of the cooperative interactions of these basic structural elements.



Several other features should be highlighted: 1) The Si (111) surface is in compression. 2) The SiC (111) C-rich face is in compression while the Si-rich face is in tension. 3) The Si (111) surface should reconstruct to some equilibrium configuration of surface Frenkel pairs. 4) The  $(\bar{2}11)$  ledge on the SiC (111) C-rich surface is the most stable. 5) The  $(2\bar{1}\bar{1})$  ledge on the Si (111) surface is the most stable due to dimer reconstruction. 6) Both ledges develop well-defined shear stress fields underneath them.

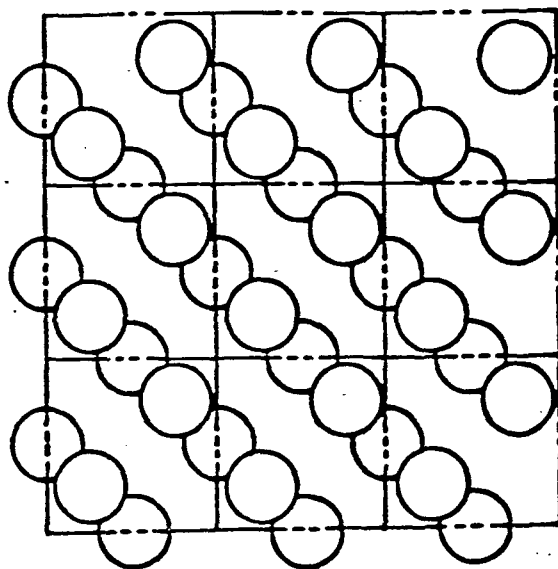
## Figure Captions

Fig. 1 Relaxed configuration of the Si (100) surface calculated at  
T = 298°K.

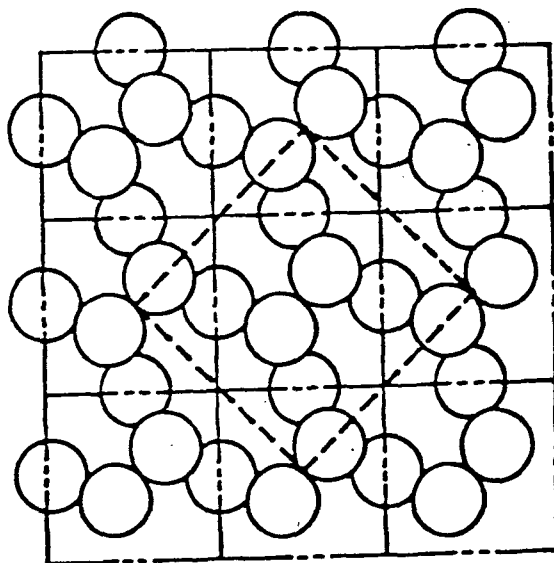
Fig. 2 (a) Side, and (b) top view of (111) surface of silicon.  
(c) Potential, and (d) surface stress distributions for layers as  
labeled in (a).

Fig. 3 Properties of  $(2\bar{1}\bar{1})$  ledge on Si (111) surface. (a) Dimer  
reconstruction. (b) Layer of atoms whose (c) potential, and (d-e)  
stresses are shown directly below. All quantities are in units of  
(eV/atom).

Fig. 4 Relaxed equilibrium geometry of surface vacancy. Also shown are  
the cradle () and hole () adatom adsorption sites.



Top view of the unrelaxed Si(100) surface



Top view of the relaxed Si(100) surface

FIGURE 1



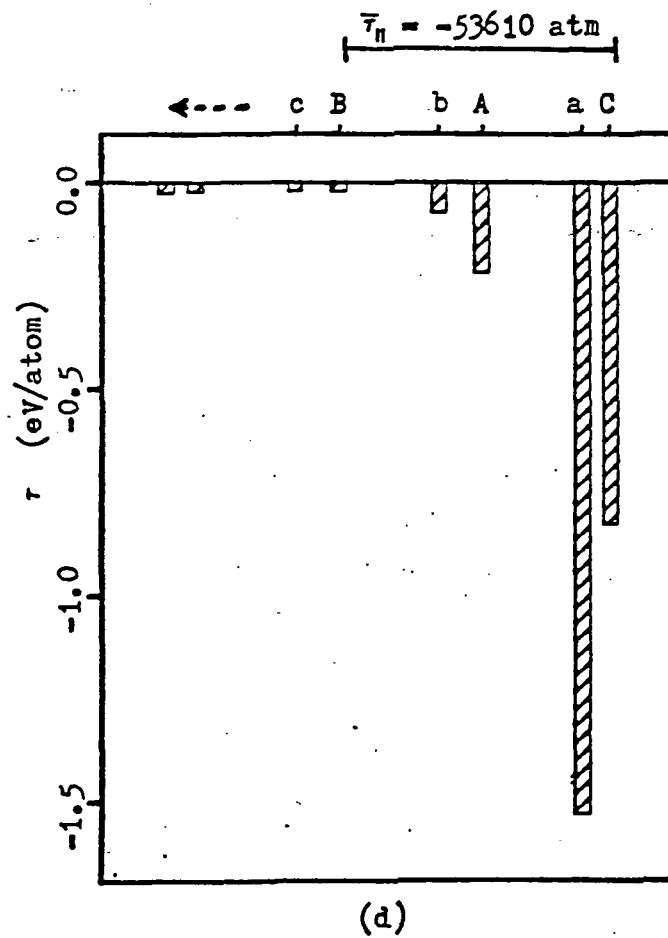
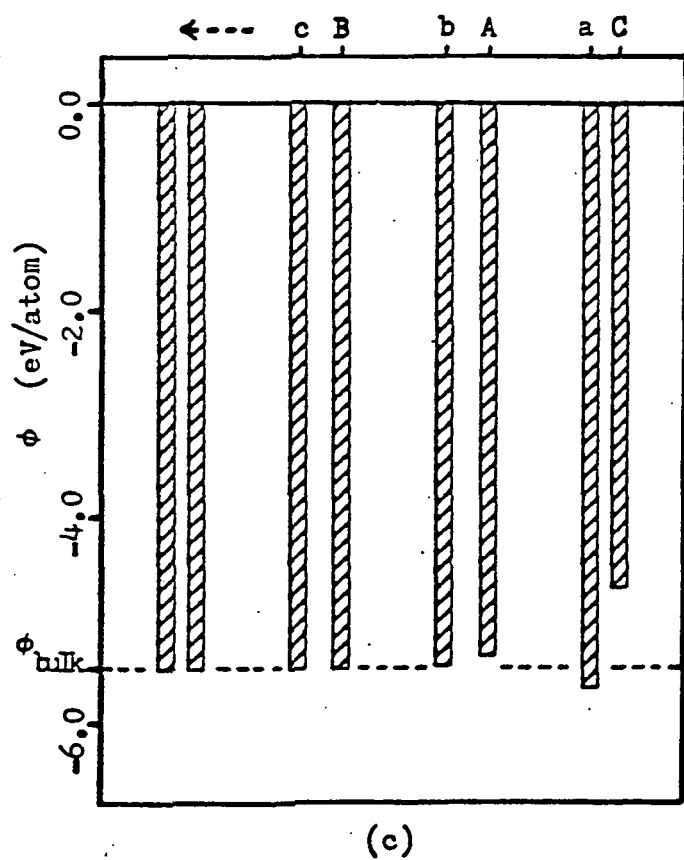
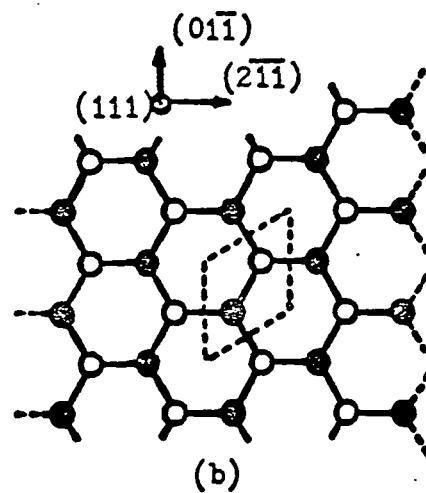
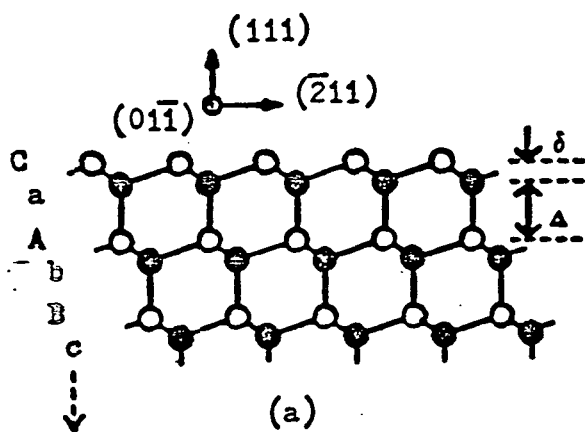


FIGURE 2

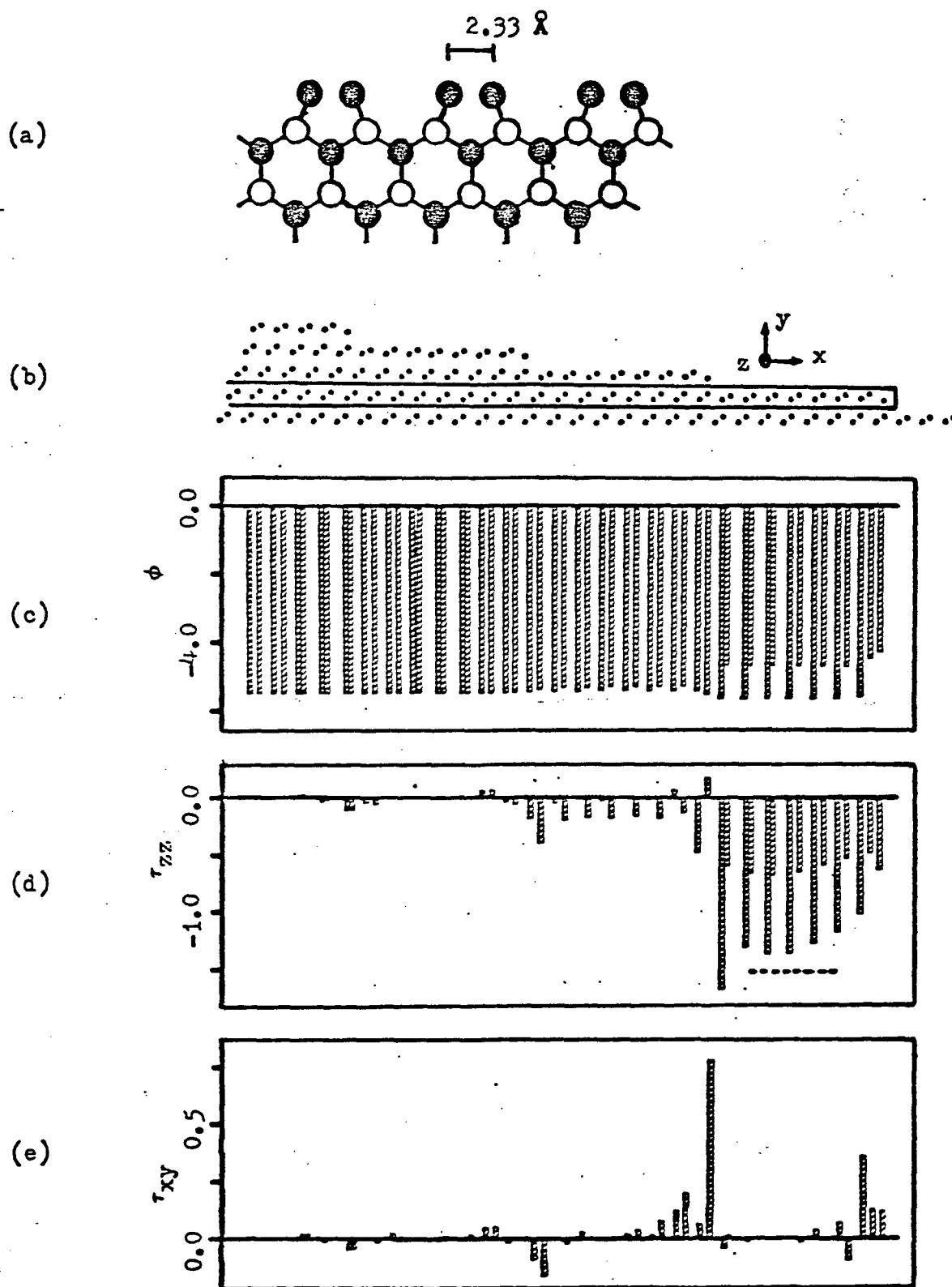


FIGURE 3

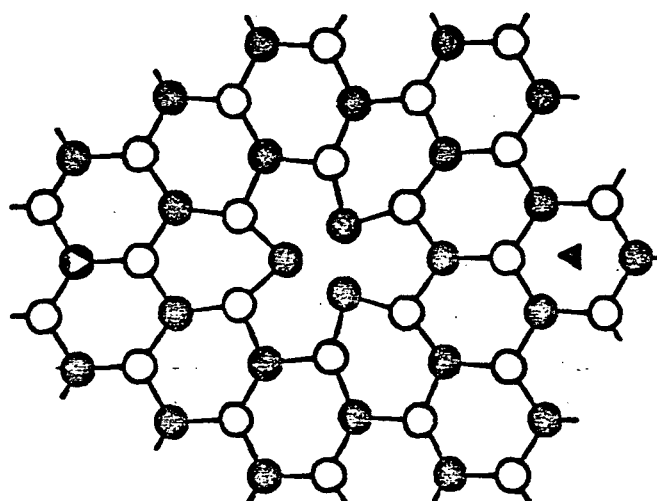


FIGURE 4

## CHAPTER VI

### Atomistic Modeling for Slip Formation

The mechanical behavior of materials can be specified by macroscopic theories on the basis of a few material constants that provide an accurate description for the responses of materials to forces. However, these theories, for example, do not provide a microscopic level of understanding of the basic mechanisms involved in plastic deformation. In general, the theories of strength of materials, elasticity and plasticity lose much of their power when the structure of a material becomes an important consideration and the material can no longer be considered a homogeneous medium [50].

The relationship between mechanical behavior and microscopic structure of materials is very important. When mechanical behavior is understood in terms of microscopic processes, it is often possible to improve the mechanical properties of a material. A microscopic description of materials, as opposed to macroscopic theories, cannot be adequately defined by using a few material constants. Instead, the system must be described in terms of interatomic forces and the coordinates of the particles which constitute the material.

Several studies based on the computer simulation of the mechanical behavior of materials exist. These studies have provided a better understanding of various mechanisms (diffusion, crack propagation, dislocation motion and plastic flow) [51,52] at the atomistic level.

Material failure is generally caused by fracture which follows yielding or plastic deformation. Slip is the simplest and the most common

example of plastic flow encountered prior to the ductile fracture of materials. In this investigation the effect of a uniaxial load exerted on a two-dimensional microscopic slab was analyzed.

The system contained 400 or more particles. Each particle was treated discretely. All particle neighbors up to  $3.5r_0$  were included in the energy force calculations. This procedure ensures that all neighbors up to the fifth-nearest neighbor will be included in the calculations. In the calculation procedure, periodic boundary conditions were not employed. This allowed us to examine the surface region reconstruction and the formation of edge dislocations during the elongation process.

Initially the system was generated in a rectangular shape in its equilibrium configuration. Then the system was elongated in a step-wise fashion by imposing a uniaxial load in small increments. After each incremental elongation, the system was allowed to equilibrate fully during a relaxation period. All the mobile particles were fully equilibrated after every incremental elongation by using a force minimization technique. The force acting on each particle was calculated; the particle was then moved in the force direction until the resultant force acting on it became virtually zero. This procedure was repeated sequentially for each moving particle up to the complete equilibration.

The discrete model used in this investigation produced results that are consistent with those from macroscopic theory. The results herein indicate that slips, which are known to be the simplest type of plastic deformation in crystalline bodies, occur predominantly on rows with a higher density of atoms (along the close-packed rows). In addition, the calculations for perfect two-dimensional triangular crystals with uniaxial

loads imposed in the  $[01\bar{1}]$ ,  $[\bar{1}\bar{1}2]$  and  $[\bar{5}14]$  directions showed that the rule of maximum resolved shear was observed [50]. These simulation results as expected are a confirmation of the macroscopic theories and illustrate the involvement of dislocations in the slip formation process.

In all cases studied, the system with point defects experienced slip formation at smaller strains than the corresponding perfect crystals. Vacancies located near the surface moved to the surface before the slip occurred. However, vacancies in the interior regions moved to the surface during the slip process.

The details of this static simulation calculation were published recently (see reference [53]).

To analyze the process of slip formation in "real time," in addition to the static approach described above, we also made use of a molecular dynamics technique. A similar model was taken into consideration and the tensile load on the system was generated in small incremental elongations. However, in this case, the system was equilibrated with a dynamic code at a finite temperature. The results obtained in this investigation were found to be basically similar to those obtained by the static method (except for a small temperature effect). This dynamic simulation provided some additional information about the involvement of dislocations in the slip formation process and its time dependent characteristics.

## CHAPTER VII

### Molecular Dynamics Calculations for Crack Propagation

In this investigation we analyzed the process of crack propagation in two-dimensional lattices using a molecular dynamics technique. Simulation calculations were carried out considering systems containing approximately 2400 discrete particles interacting via two-body potentials. In addition to energetics, forces and instantaneous position vectors, we also calculated stress components for every particle in the system. General characteristics of the model considered in this study are basically similar to the one used in the previous chapter for the slip formation calculations.

Simulations for two-dimensional systems are relatively easier to analyze than results for three-dimensional systems. First of all, 2D systems contain a smaller number of particles and, therefore, require less computer time. Results can be represented by simple 2D plots and problems arising due to the multi-particle character of the system are easily identifiable. Thus, the analysis of the 2D system provides considerable information not only about the microscopic nature of the crack growth phenomenon, but also provides some knowledge about "how to interpret the simulation results." The question of the credibility of these 2D results, of course, remains unanswered. At this stage, it is not known how to extrapolate results obtained from a 2D simulation to a 3D domain. However, the results obtained in this study together with several other reports [54,55] in the literature indicate that 2D systems, in most cases, do exhibit characteristics similar to 3D systems.

Atomistic level analysis of the crack propagation process using computer simulation techniques has been the subject of several earlier investigations. In the literature we could find only a few reports relevant to the study carried out in this investigation. In the report by Ashurst and Hoover [54], the fracture phenomenon was investigated based on a truncated Hook's law force. They have found that, even with this very simplistic force law, their static simulation furnished results for energy, entropy, stress concentration and crack structure all to be consistent with expectations from macroscopic elastic theory.

The other relevant and more recent study was reported by Dienes and Paskin [55]. In this modeling study they also considered a 2D triangular lattice with particles interacting via the Lennard-Jones function. A crack has been introduced in the interior of a pre-stressed sample. The crack was initiated by "cutting" the bonds between a given number of atoms at the central portion of the sample. The interatomic potential was artificially set to zero between these atoms. According to their report, the condition would correspond to the insertion of a very thin knife to create the crack. Furthermore, in the energy and force calculations, they only considered nearest neighbor interactions (by taking  $R_{\text{cut}} = 1.6 r_0$ ). In their model, the crack was aligned parallel to close-packed rows and displayed a linear path in its propagation. Finally, they found that their results are quantitatively good at the early stages of the propagation process.

The main objective of this study is to investigate the crack propagation phenomenon at an atomistic level to understand and resolve various mechanism involved in a crack tip process. In the first part of this



simulation study (to test the system under consideration) we calculated the stress-strain characteristics of a perfect two-dimensional lattice at a finite temperature. This calculation was carried out primarily for comparison with the results obtained in the second part of the study where calculations were performed for systems with pre-existing cracks.

(i) Perfect Lattice:

As a perfect 2D lattice, the basal plane of an hcp lattice was taken into consideration. A system of 2400 particles in a rectangular shape ( $80 \times 30$ ) was first generated in static equilibrium. A tensile load was applied in the  $[112]$  direction, which is the close-packed direction. This direction was also chosen as the  $x$ -direction in our cartesian coordinate system. The load was imposed in small incremental strains (in this case elongations) of 0.01. This was performed uniformly throughout the system by factorizing all the  $x$ -components of the position vectors describing the system. In the  $x$ -direction, periodic boundary conditions (PBC) were applied to provide continuity for the system (in the tensile direction), and also to furnish two free surfaces in the  $y$ -direction. In a general sense, the imposed PBC provides the desired tensile strain on the system.

The system was relaxed after every incremental strain by a molecular dynamics code. A cut-off radius,  $R_{\text{cut}}$ , of  $2.86 r_0$  was considered for the energy and force calculations. This  $R_{\text{cut}}$  is between the fourth and fifth neighboring shells surrounding the central atom and provides approximately 30 neighbors. The reduced time step was taken as 0.01 and the reduced temperature was  $T^* = 0.02$  (to compare with real systems; e.g., for copper these represent  $2.5\text{E-}15$  seconds and  $100^\circ\text{K}$ , respectively).

For every strain value, the stress components of particles were estimated as derivatives of the potential energy per particle. The interaction energy for a particle  $i$  was calculated as:

$$\phi_i = \sum_j^M u(r_{ij}) \quad (18)$$

where  $M$  is the total number of neighbors of atom  $i$  and  $r_{ij}$  denotes the distance between particles  $i$  and  $j$ . To represent the pair interactions we employed the Lennard-Jones function:

$$u(r_{ij}) = \epsilon \left[ \left( \frac{r_0}{r_{ij}} \right)^{12} - 2 \left( \frac{r_0}{r_{ij}} \right)^6 \right] \quad (19)$$

with  $\epsilon$  and  $r_0$  denoting the energy and the internuclear distance, respectively, at equilibrium.

For each particle the stress components were calculated considering Lagrange strain parameters. For example, the stress component, for a particle  $i$ , in the  $x$ -direction is given by:

$$\sigma_{xx}^i = \frac{6\epsilon}{a_0} \sum_j^M \left[ \left( \frac{r_0}{r_{ij}} \right)^{12} - \left( \frac{r_0}{r_{ij}} \right)^6 \right] \left( \frac{x_i}{r_{ij}} \right)^2 \quad (20)$$

where  $a_0$  denotes the area per particle and  $x_i$  is the  $x$ -component of the position vector for the particle  $i$ .

The calculated stress-strain curve for the perfect lattice case is shown in Fig. 1, up to  $e \approx 0.09$ .

### (ii) 2D Lattice with an Existing Crack

A lattice with an initial surface crack was generated by removing 9 particles from the surface region of a perfect lattice (see Fig. 2). This system, now with an existing surface crack, was elongated and relaxed by the molecular dynamics code in a similar way explained above for the perfect case. First, the effect of the temperature on the stress-strain curve was analyzed up to  $e = 0.03$ . Figure 3 shows two curves, dotted and solid, representing the stress-strain curves for  $T^* = 0.1$  and  $T^* = 0.02$ , respectively. The shift in the dotted curve (high temperature curve) is mainly due to the thermal expansion. For lower strain values, these curves represent fully equilibrated systems. However, for strains higher than 0.02, systems may require additional relaxation times to equilibrate completely. The difficulty involved in attaining the equilibrium is mainly due to large fluctuations displayed by the stress values calculated as derivatives of the energy. At this stage, we believe that the general trend exhibited by these two curves is sufficiently accurate for the present investigation. Any further incremental elongations (in addition to  $e = 0.03$ ) cause the crack to propagate. Determination of the critical strain, i.e., the strain at which the crack first starts to propagate, is difficult to assess. For this purpose we performed three separate runs with three different pre-strained systems, namely with  $e = 0.03$ ,  $e = 0.035$  and  $e = 0.04$ , all at  $T^* = 0.02$ . The 2D lattice with the surface crack was strained in one single step from its original length up to 3.0, 3.5 and 4.0% elongations. In the case of  $e = 0.03$ , the crack did not exhibit any growth and the overall configuration of the systems remained unchanged up to 3500 time steps. However, for both  $e = 0.035$  and 0.04 cases, the

propagation of the crack took place. In these prestrained cases, we simulated the system under nonequilibrium isothermal conditions. For the  $e = 0.035$  case, the crack growth first initiated after 1000 iteration steps. Figure 4 displays the stages of this relaxation process up to 3200 iterations, at which the system reached almost to an equilibrium state. The darker circles in the figures represent particles with higher stresses. For the  $e = 0.04$  case, on the other hand, the crack propagated much earlier (obviously because of the high strain imposed initially). The crack started growing first at the 500th iteration step and the system attained an equilibrium state at approximately 2400 iteration. The stages of this propagation process are shown in Fig. 5. Again, the darker circles display particles with higher stresses. In both cases, the particles at the crack tip exhibited high stresses consistently. Furthermore, the crack propagated along the close-packed rows of the lattice and, at the same time, tried to remain perpendicular to the applied load by choosing a zig zag path. These behaviors are very much consistent with experiments and theories based on macroscopic considerations and, therefore, indicate the adequacy of the present atomistic level simulation procedure. The relaxation of the system can be followed in Fig. 6 where the average stress is plotted versus the iteration steps. The oscillatory behavior of this curve is a temperature effect mainly due to vibrational motions displayed by individual particles in the system. From the snapshots shown in Fig. 5, we also calculated the velocity of the crack propagation. The curve in Fig. 7 represents the variation in the crack propagation velocity as a function of the calculated average stress. The upper range of this curve is near the velocity of sound propagation. This is expected according to a report by Ashurst and Hoover [54].

## Figure Captions

Fig. 1 Stress-strain curve for the perfect lattice.

Fig. 2 Two dimensional lattice with an existing surface crack.

Fig. 3 Temperature effect on the stress-strain curve.

Fig. 4 Snapshots for the crack propagation with  $e = 0.035$ .

Fig. 5 Snapshots for the crack propagation with  $e = 0.040$ .

Fig. 6 Variation of the averaged stress as a function of time steps.

Fig. 7 Crack propagation velocity plotted versus the averaged stress.

# STRESS-STRAIN CURVE

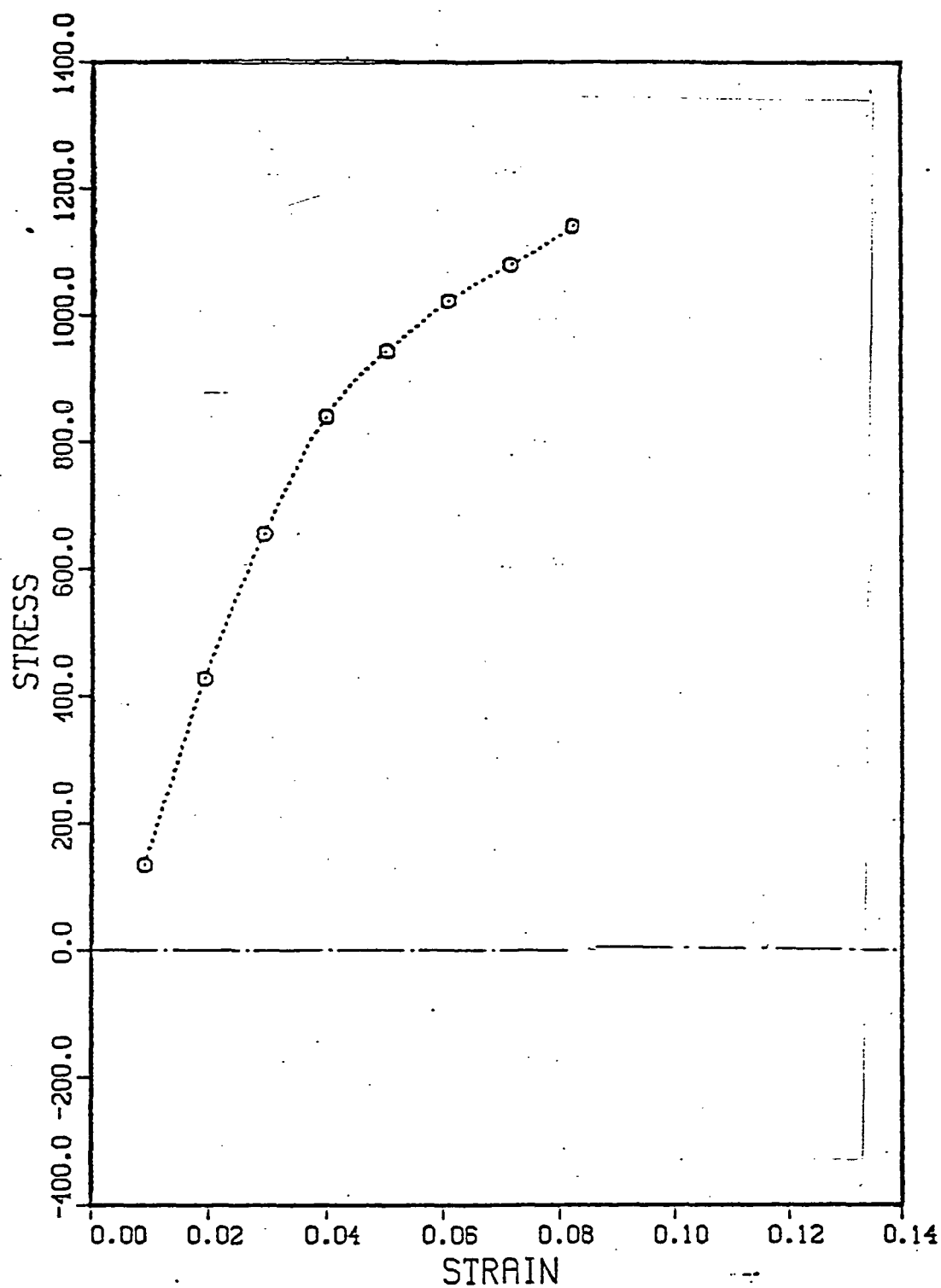
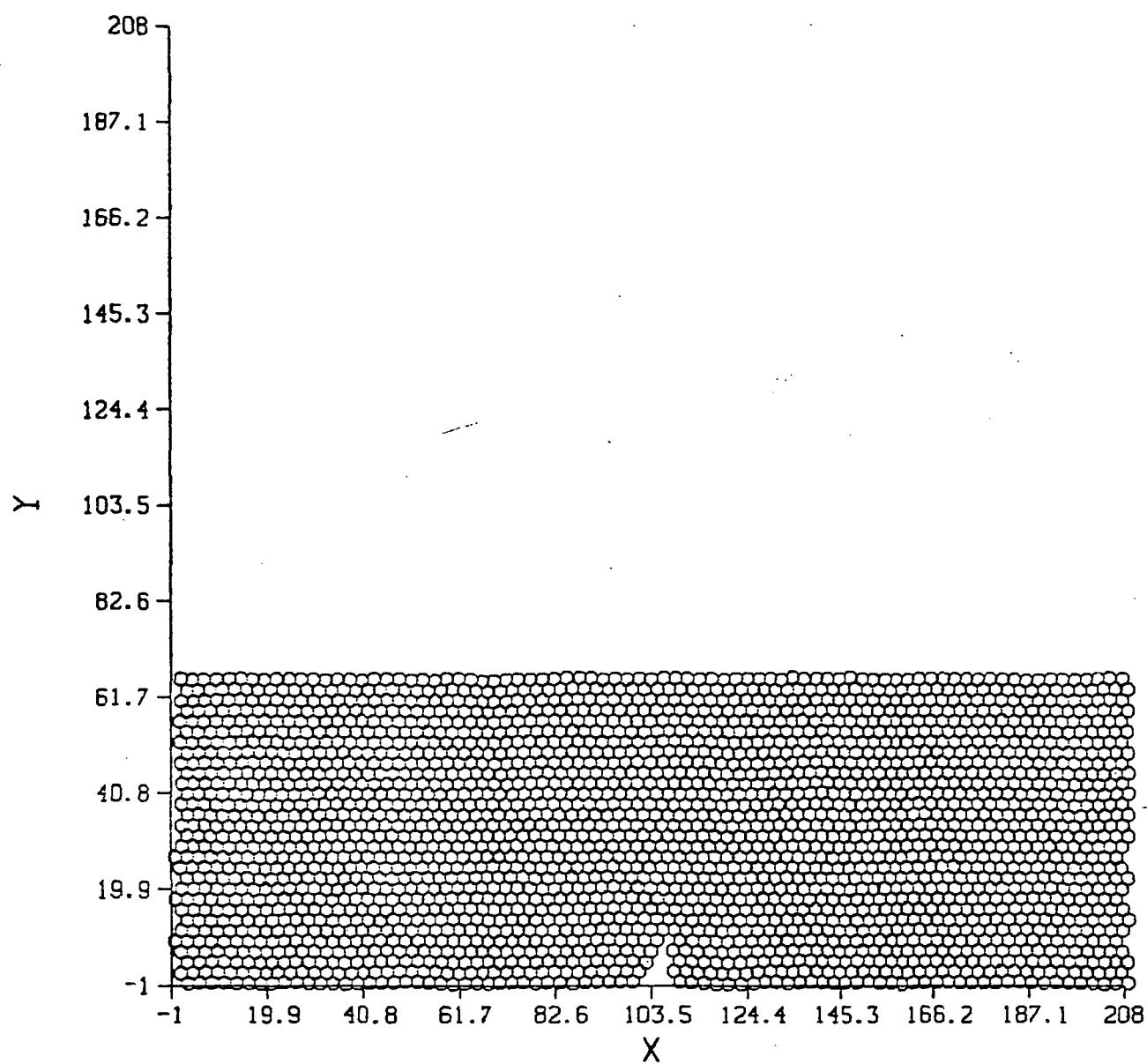


FIGURE 1.



o - -0.91 TO 0.55 2391 PTS

STEP= 200

FIGURE 2

# TEMPERATURE EFFECT ON THE STRESS-STRAIN CURVE

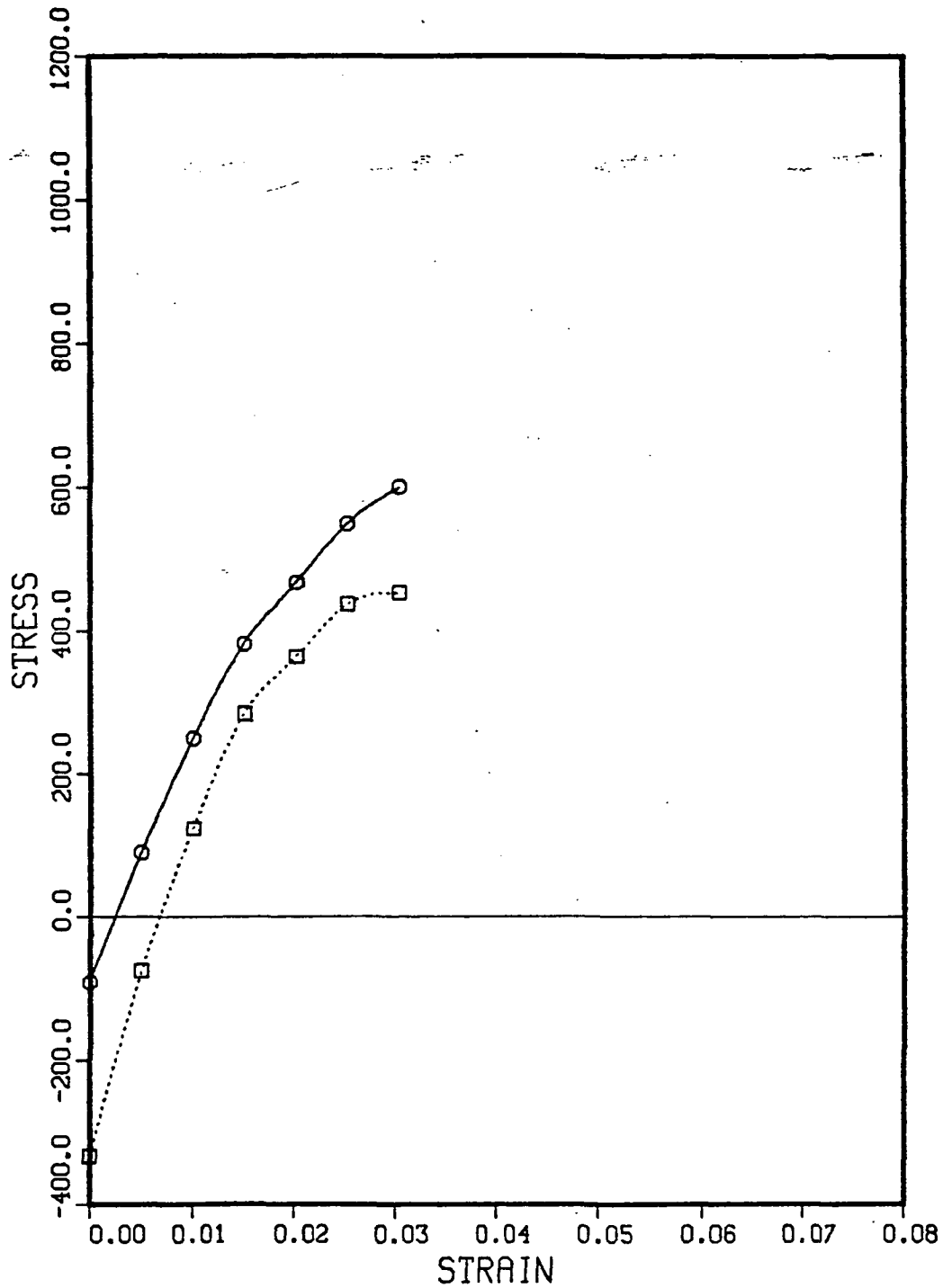
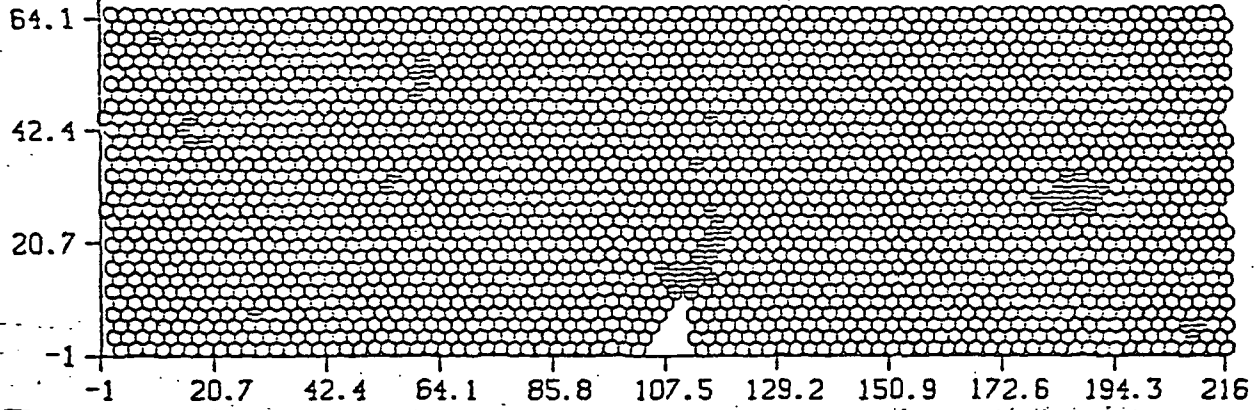


FIGURE 3

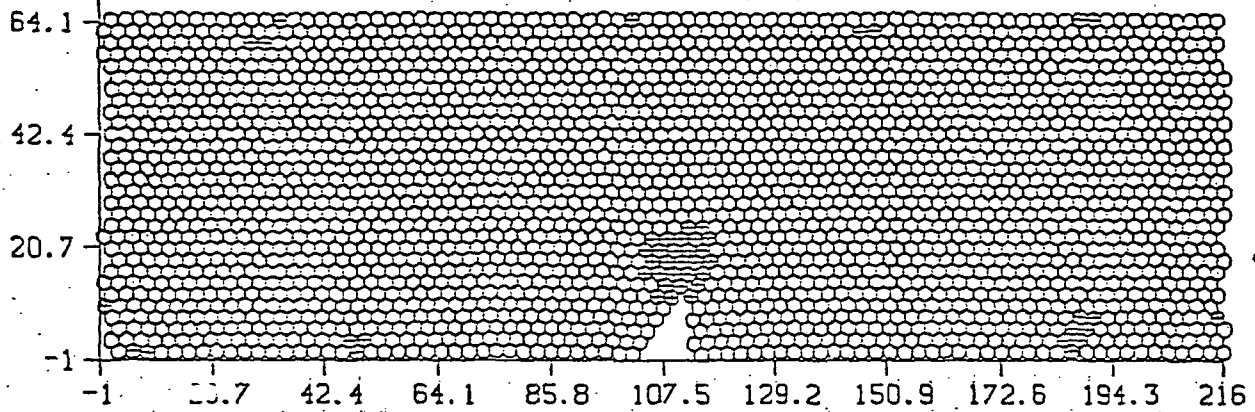


ORIGINAL PAGE IS  
OF POOR QUALITY

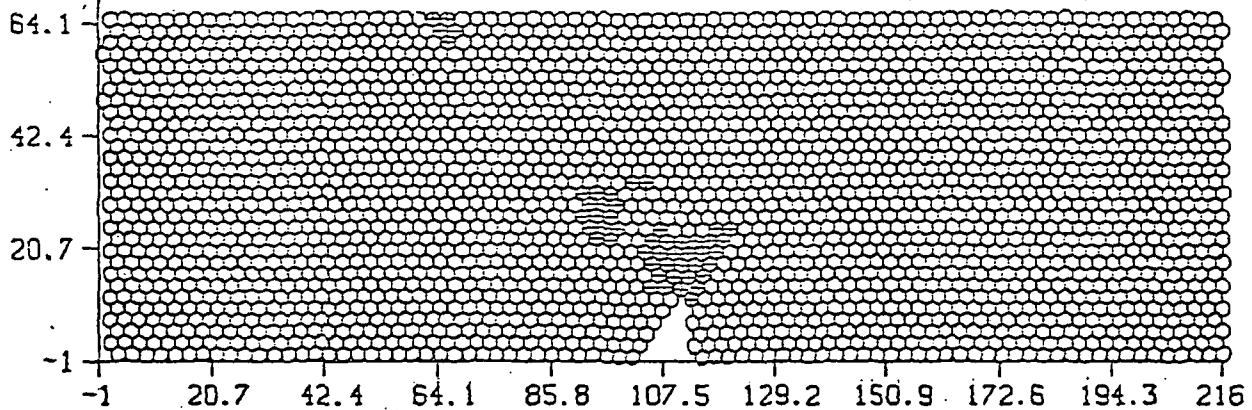
ORIGINAL PAGE IS  
OF POOR QUALITY



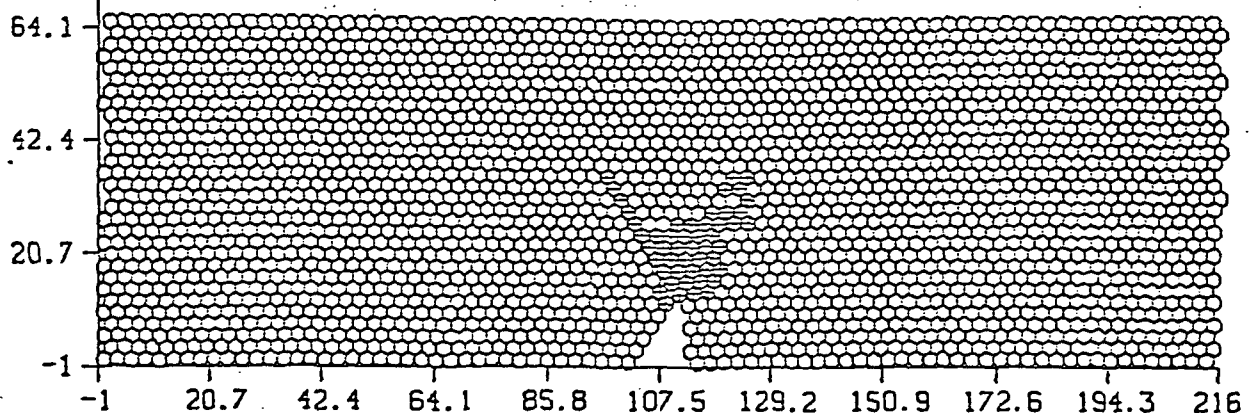
200



400



600



1000

FIGURE 4

ORIGINAL PAGE IS  
OF POOR QUALITY

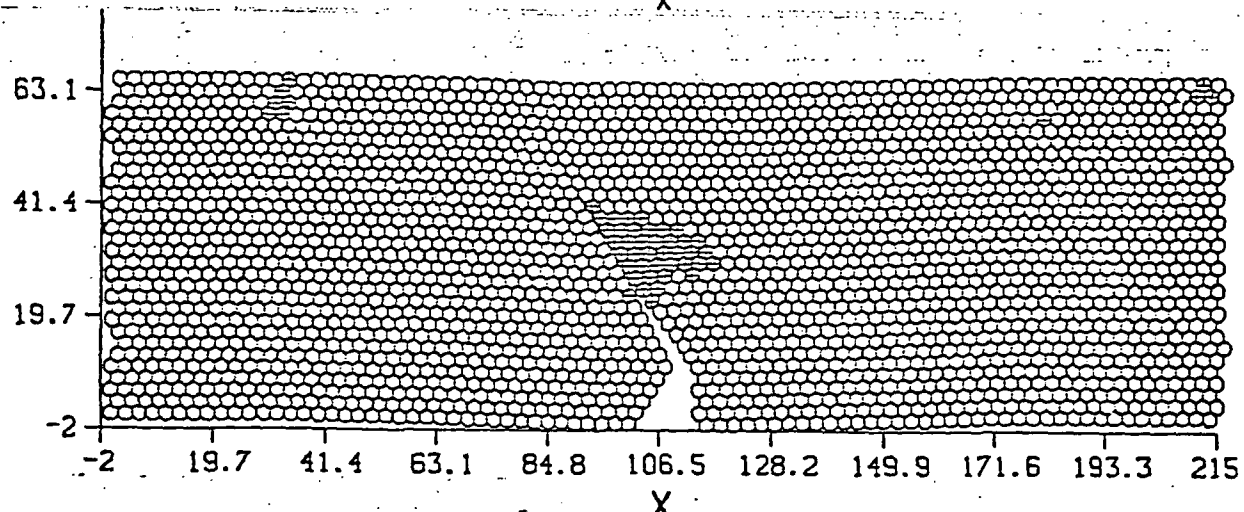
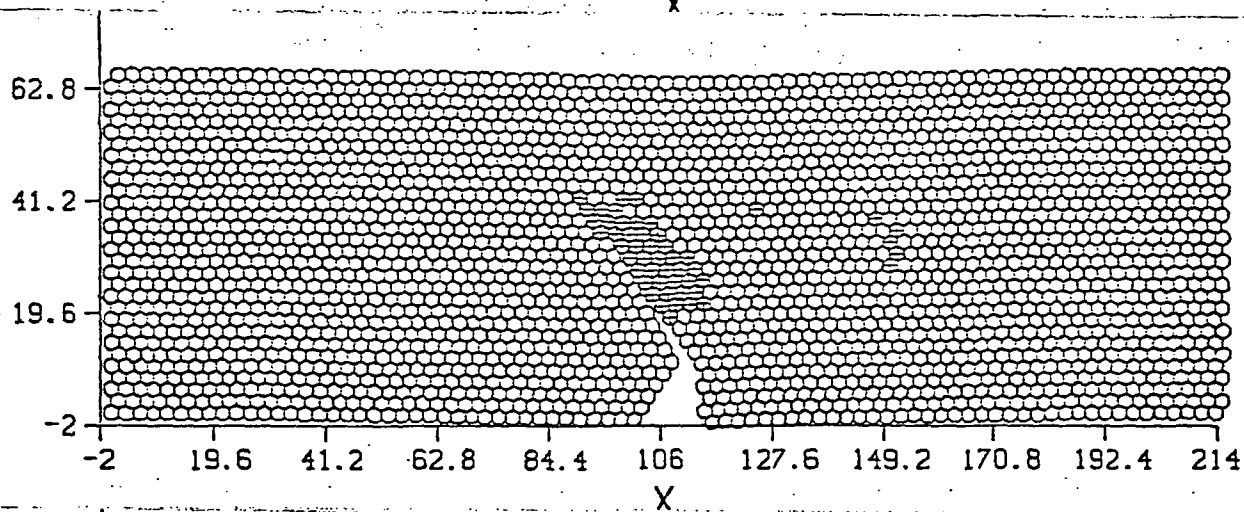
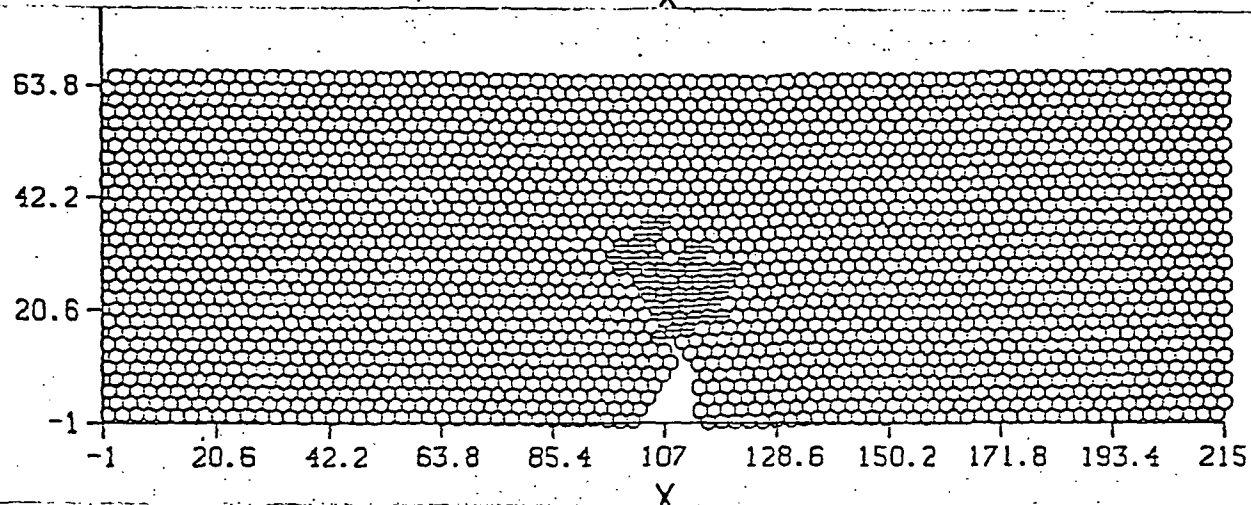
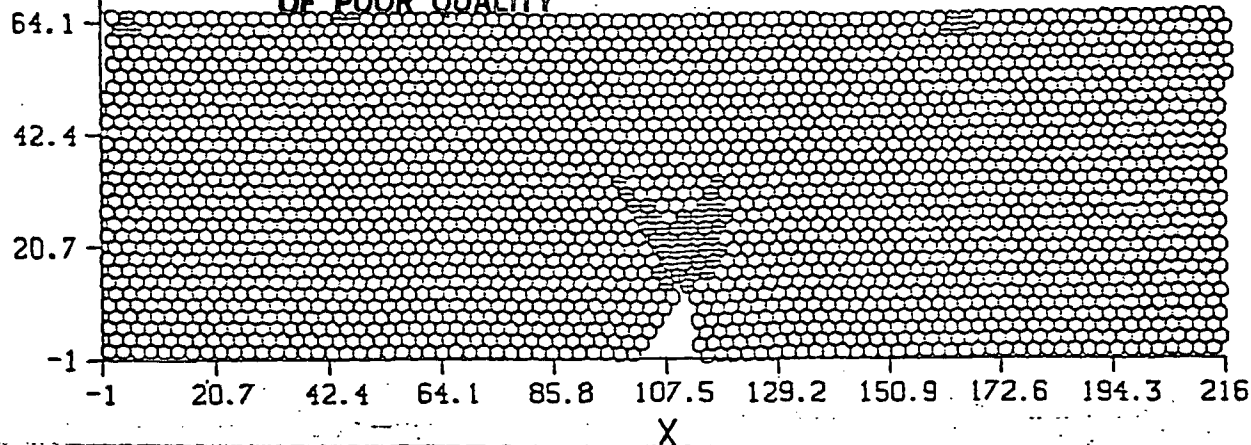
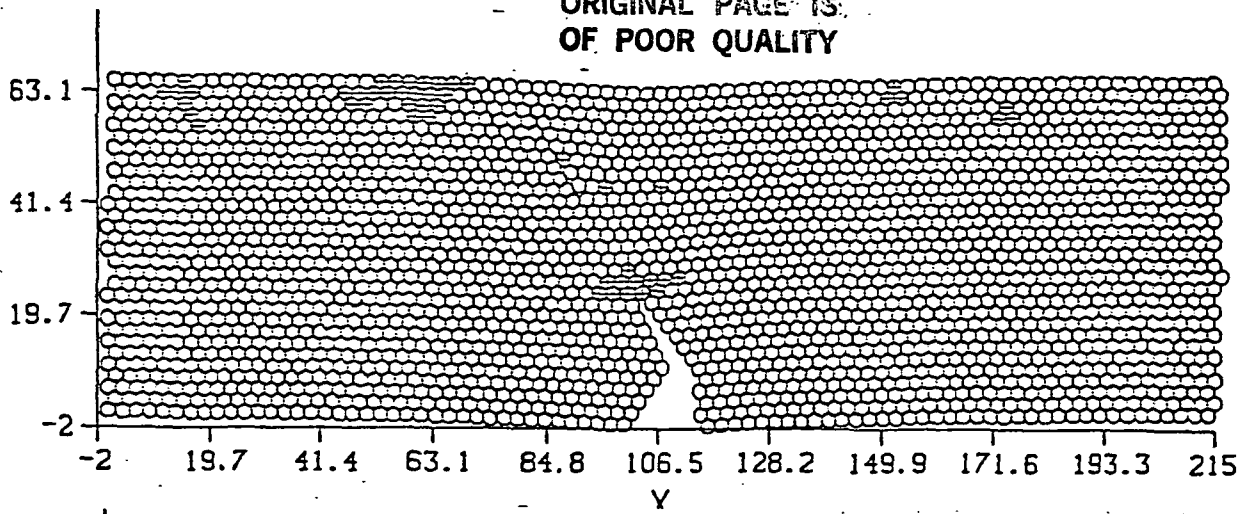
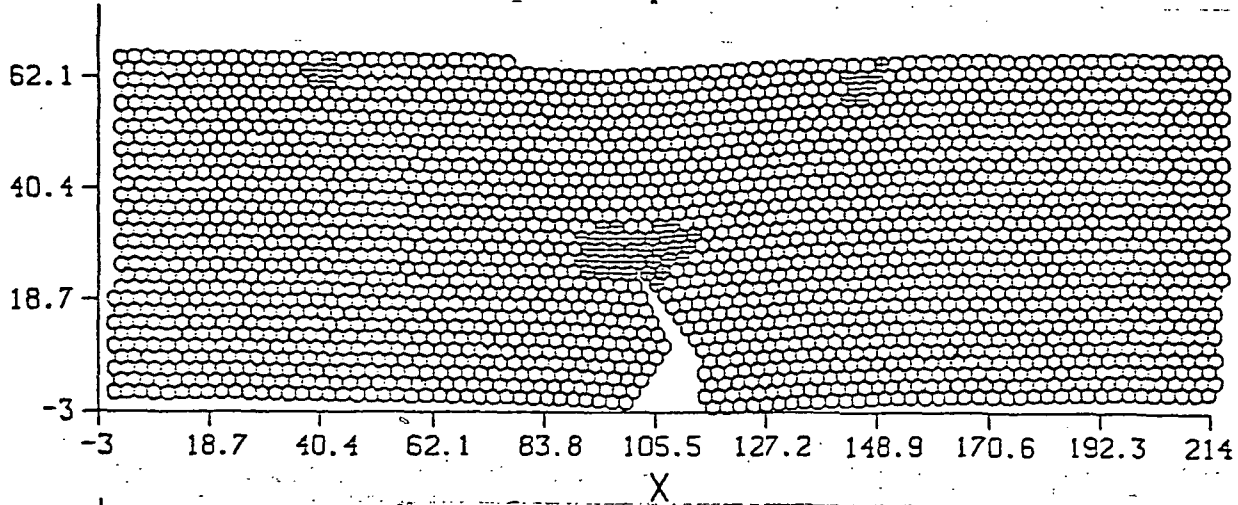


FIGURE 4 (cont'd)

ORIGINAL PAGE IS  
OF POOR QUALITY

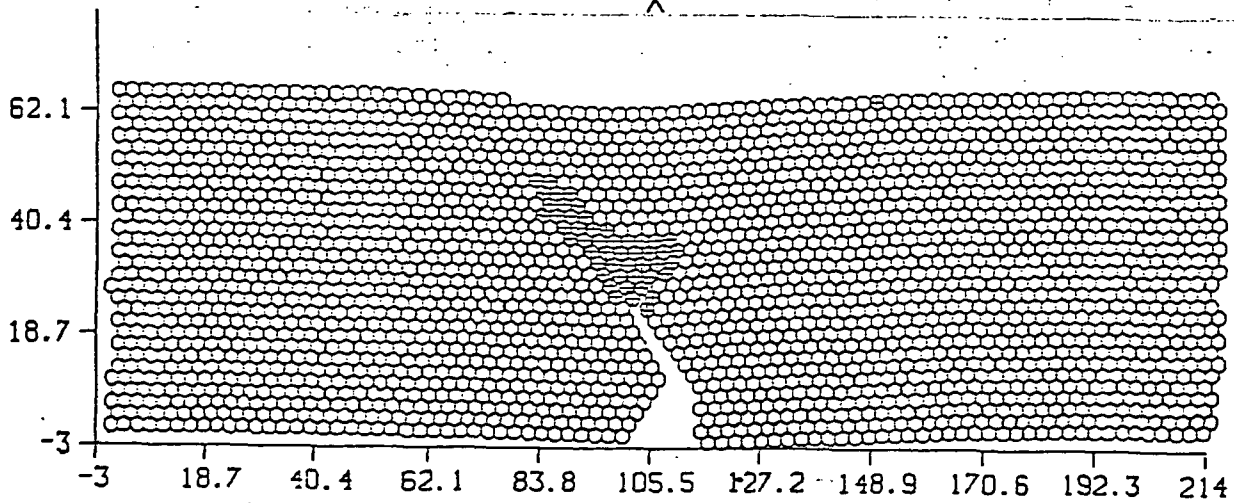


2000

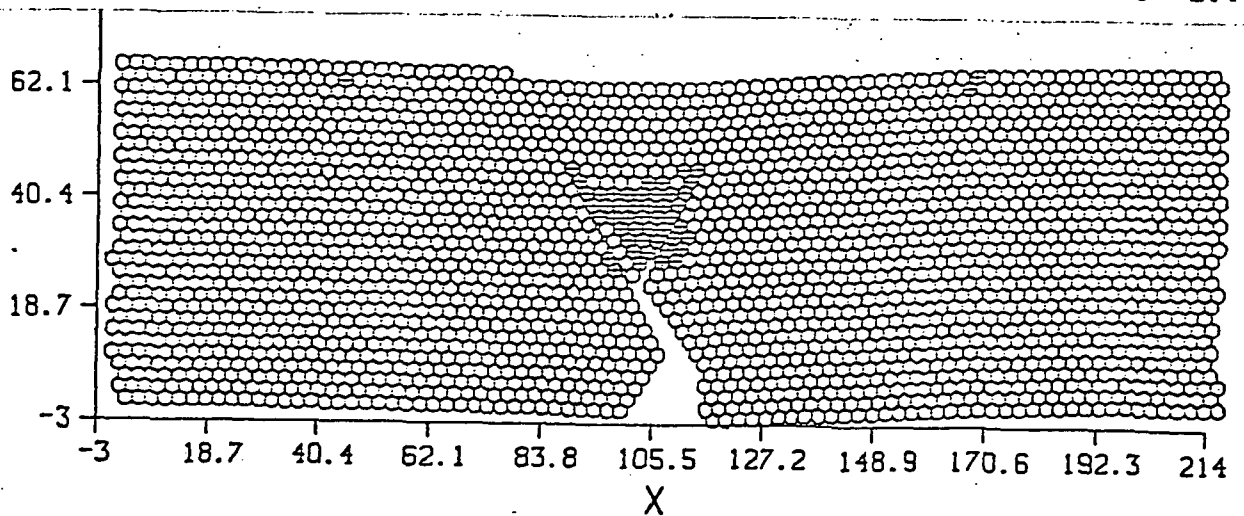


2200

FIGURE 4 (cont'd)



2400



2600

ORIGINAL PAGE IS  
OF POOR QUALITY

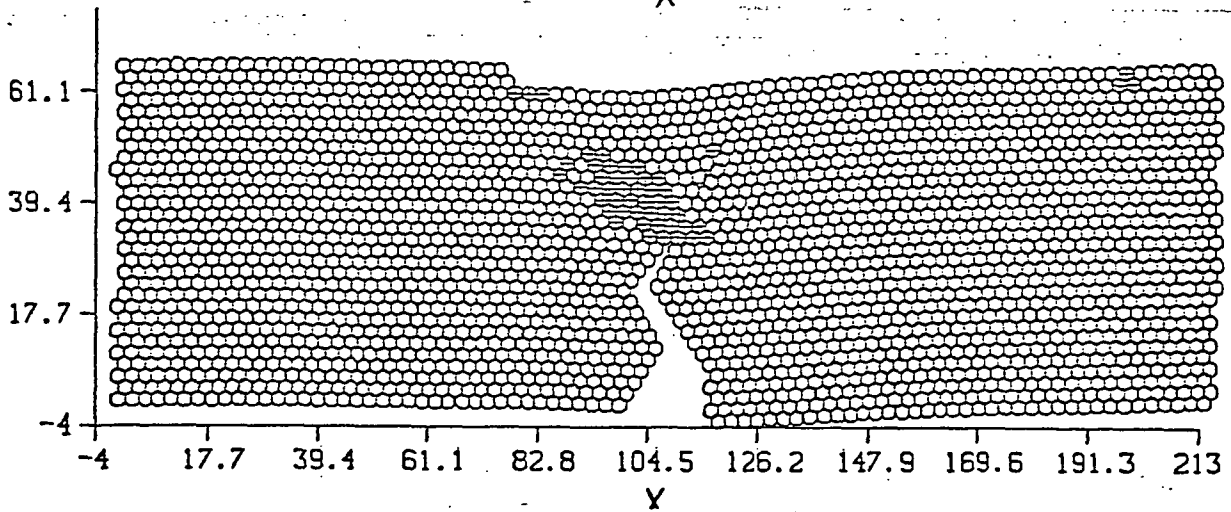
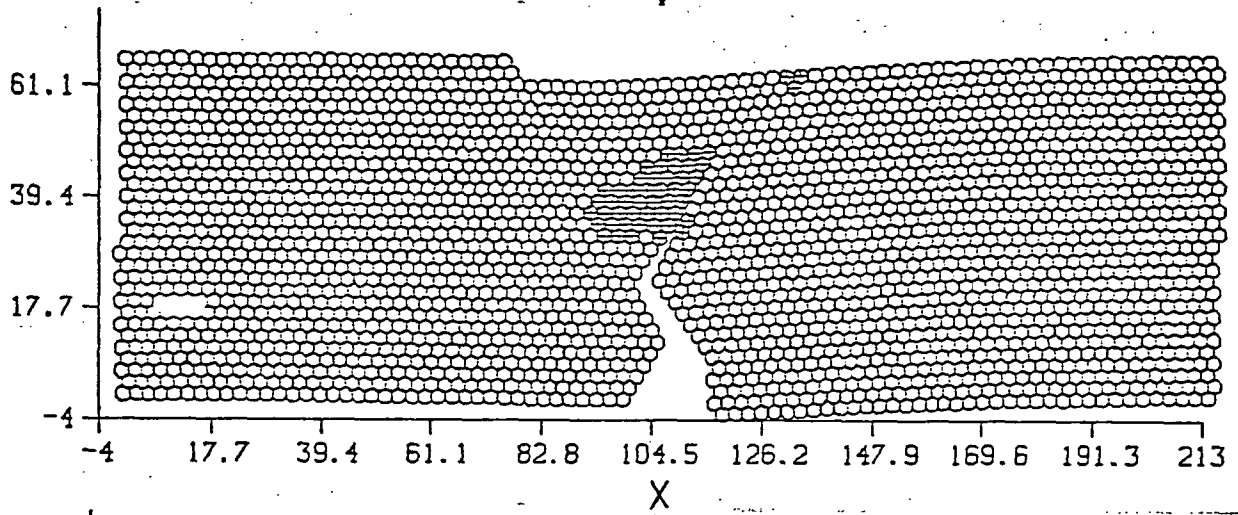
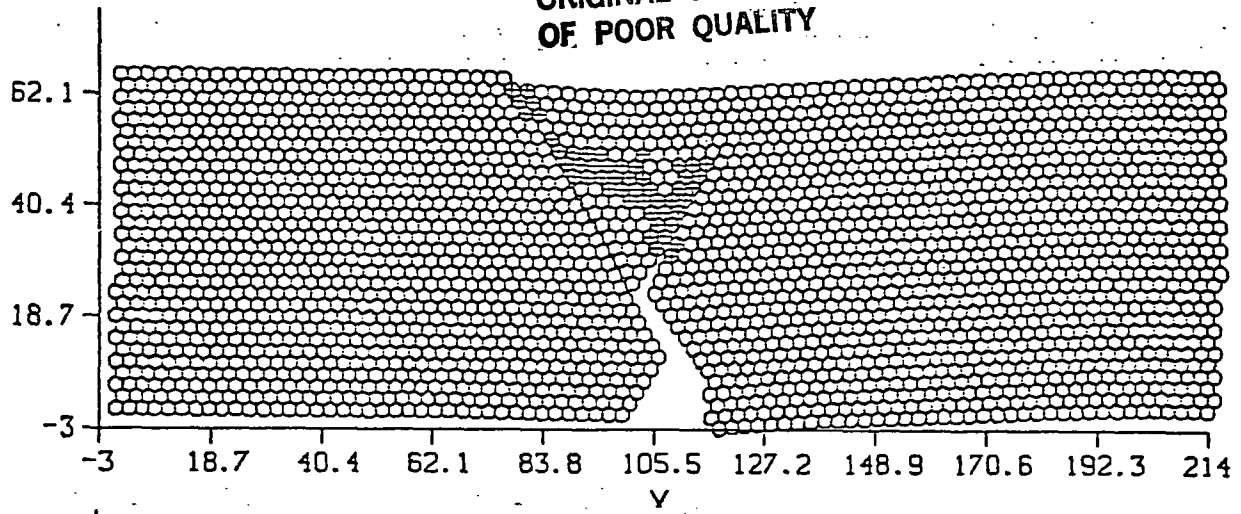
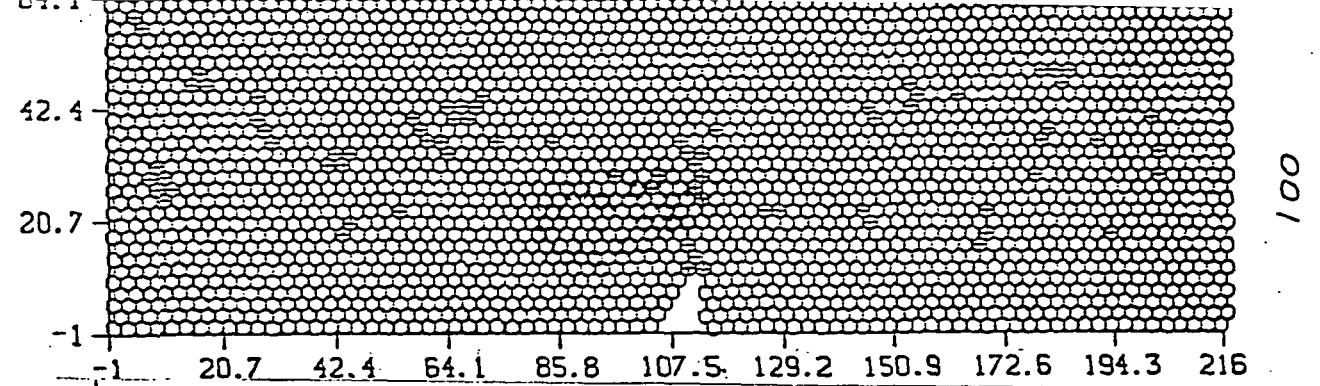
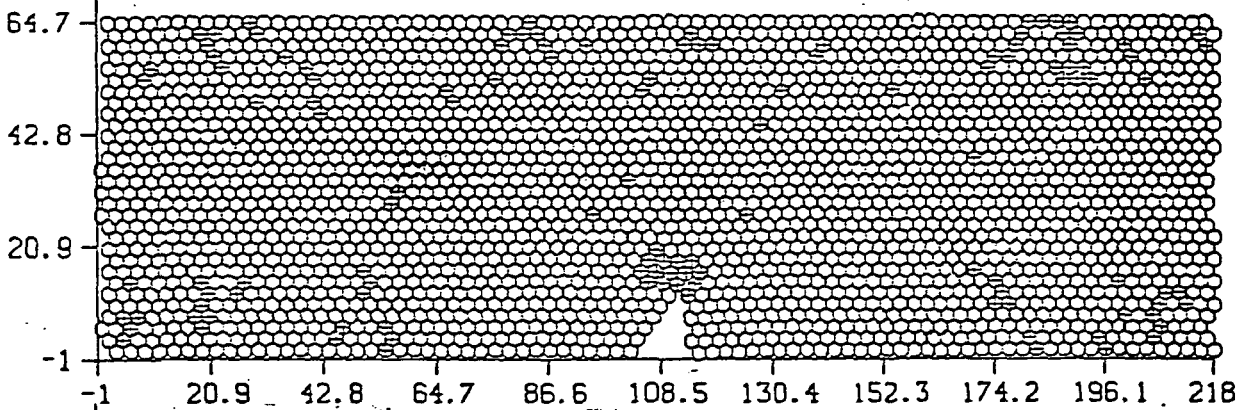


FIGURE 4 (cont'd)

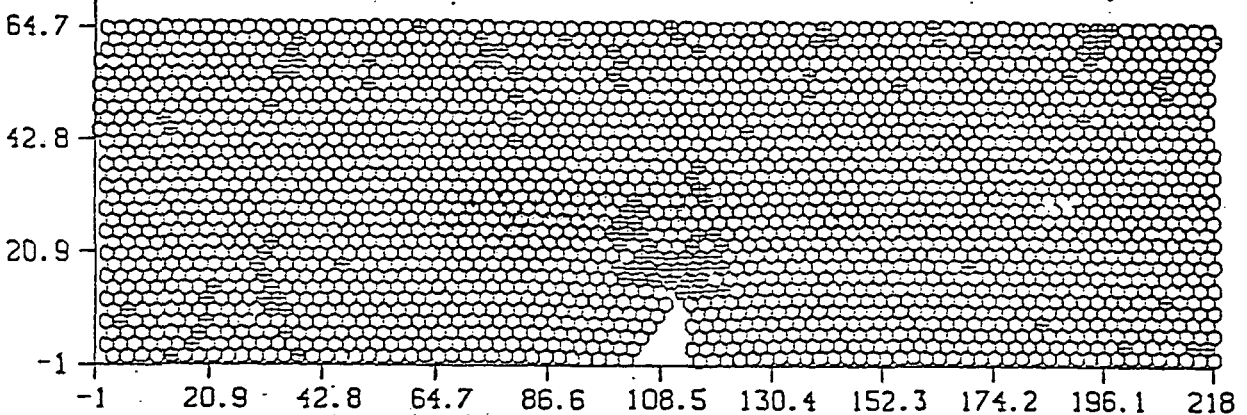
ORIGINAL PAGE IS  
OF POOR QUALITY



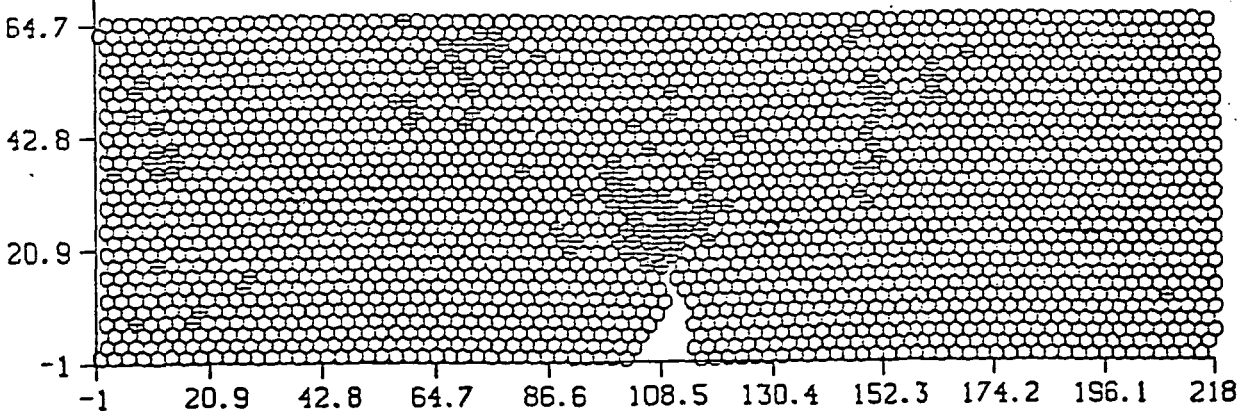
100



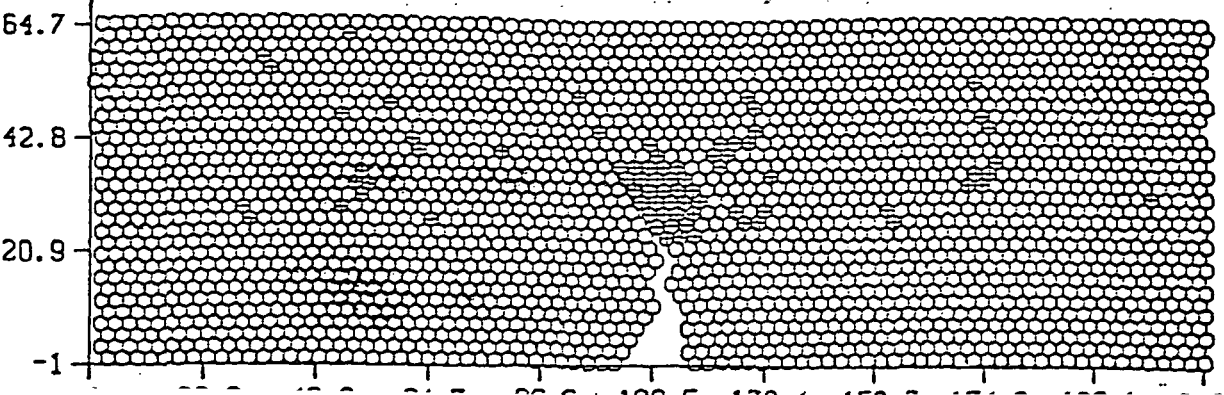
300



500



700

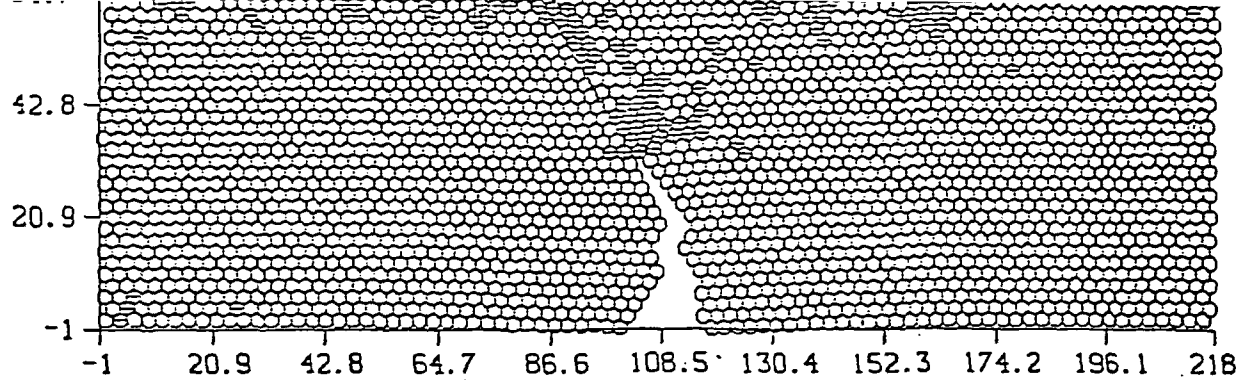


900

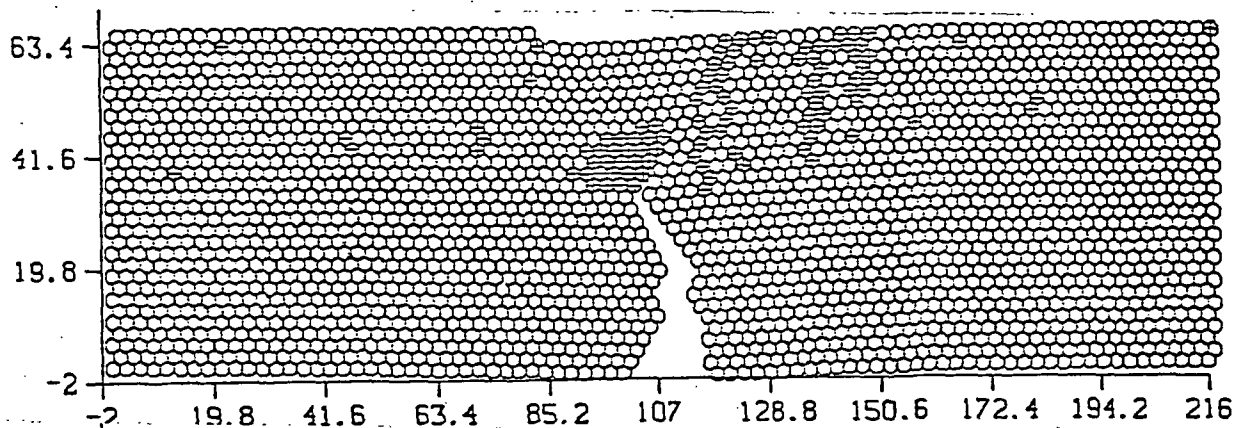
FIGURE 5



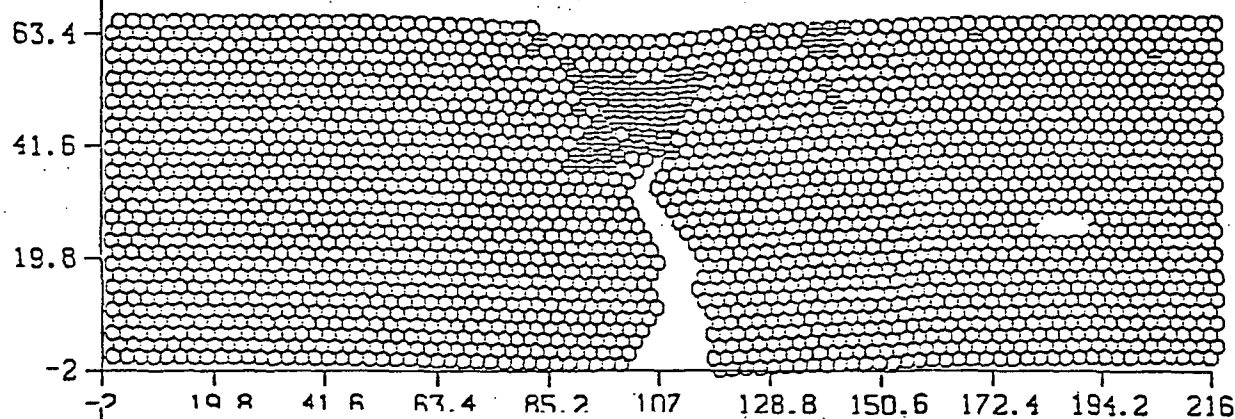
ORIGINAL PAGE IS  
OF POOR QUALITY



1200

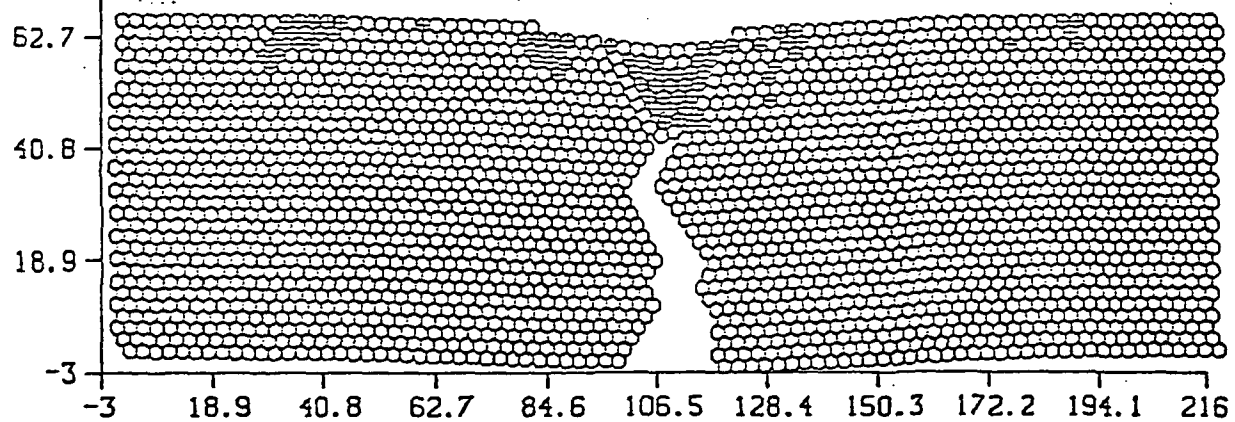


1400

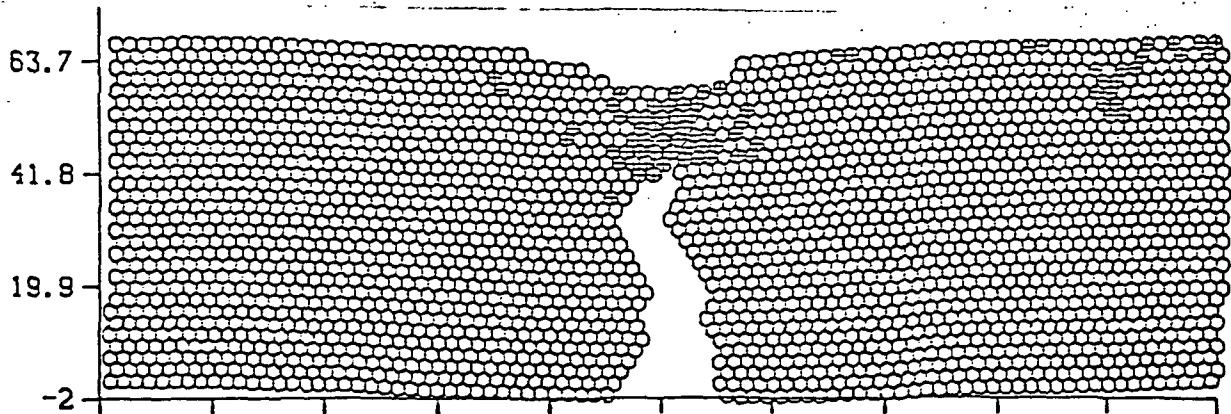


1600

FIGURE 5 (con'd)



1900



2400

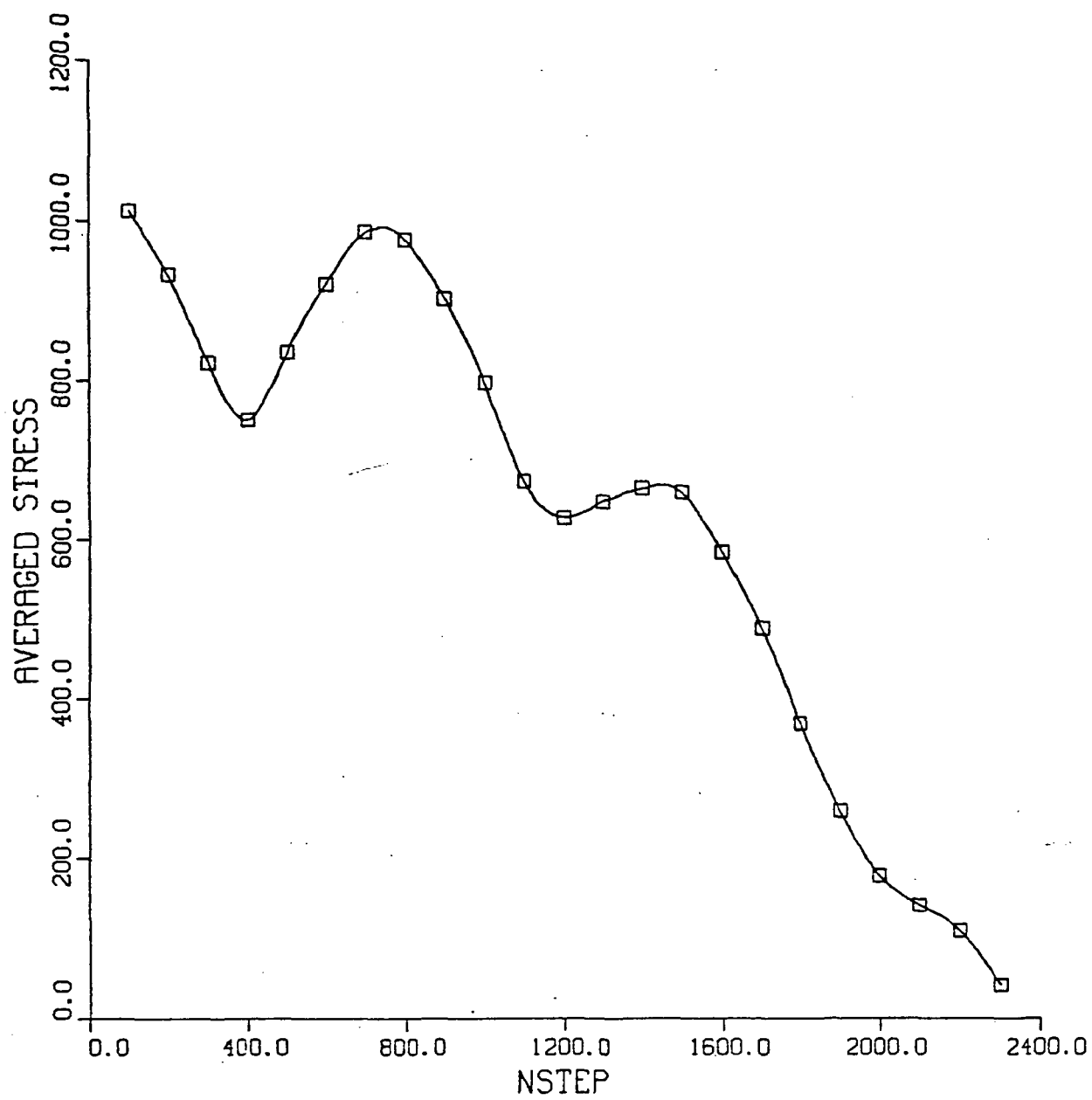


FIGURE 6

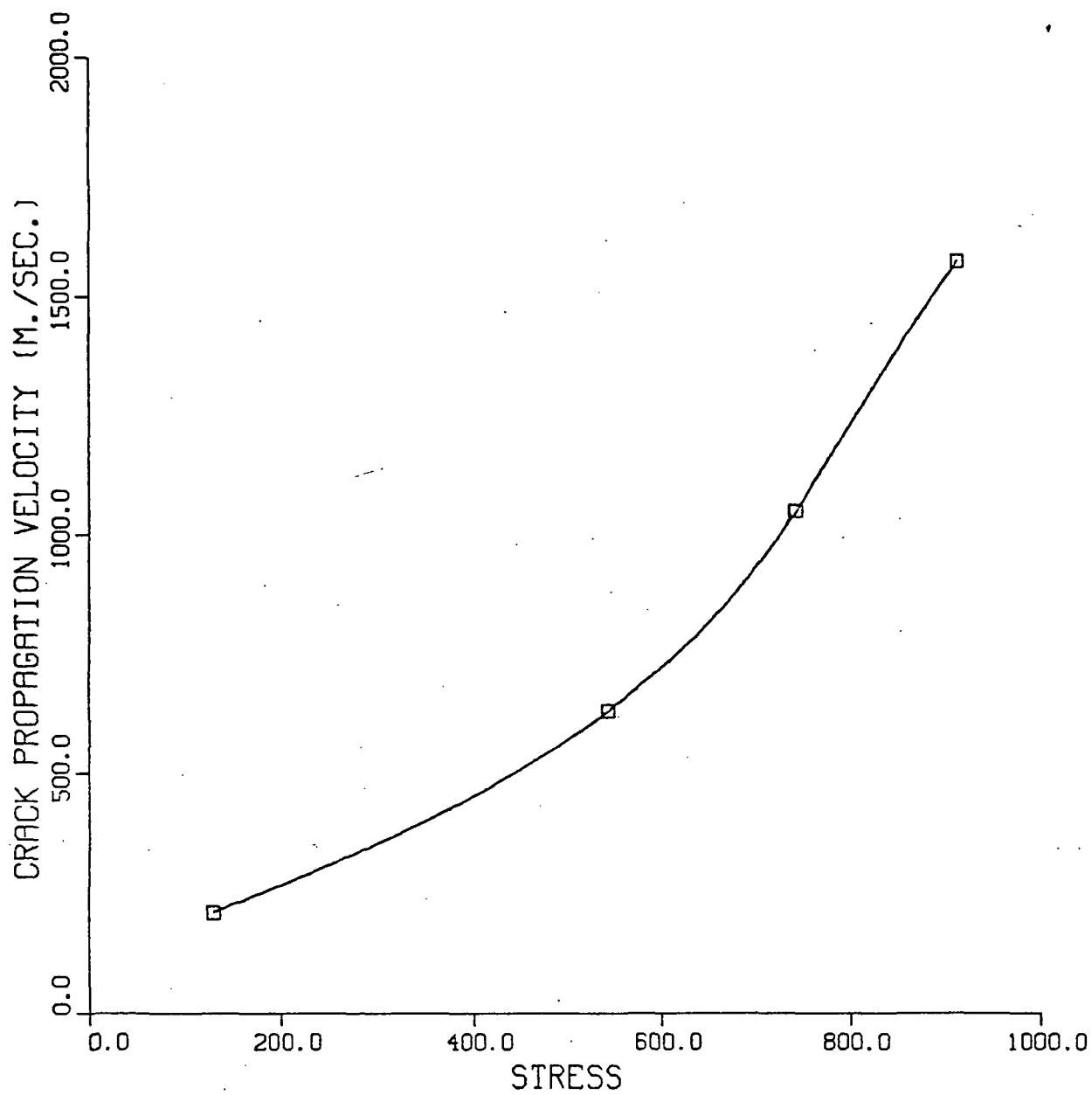


FIGURE 7



## References

- 1) "Computer Simulation for Materials Applications," Ed: R.J. Arsenault, J.R. Beeler and J.A. Simmons, Nuclear Metall. 20 (1976).
- 2) F.F. Abraham, J. Vac. Sci. Technol. B2, 534 (1984).
- 3) "Atomistics of Fracture," Ed: R.M. Latanision and J.R. Pickens (Plenum Press, New York, 1983).
- 4) W.W. Wood and J.J. Erpenbeck, Ann. Rev. Phys. Chem. 27, 319 (1976).
- 5) T. Halicioğlu, Phys. Stat. Sol. (b) 99, 347 (1980).
- 6) M.B. Doran and I.J. Zucker, J. Phys. (c) 4, 307 (1971).
- 7) R.J. Bell and I.J. Zucker, "Rare Gas Solids," Eds: M.L. Klein and J.A. Venables (Academic Press, 1976), Ch. 2.
- 8) T. Halicioğlu and P.J. White, J. Vac. Sci. Technol. 17 (1980); and Surf. Sci. 106, 45 (1981).
- 9) G.A. Ozin, Fara. Symp Chem. Soc. "Diatomic Metals and Metallic Clusters" 14, 1 (1980).
- 10) J.F. Hamilton, J. Vac. Sci. Technol. 13, 319 (1976); and, G. Apai, J.F. Hamilton, J. Stohr and A. Thompson, Phys. Rev. Lett. 43, 165 (1979).
- 11) "Metal Bonding and Interactions in High Temperature Systems," Ed: J.L. Gole and W.D. Stwallly (Am. Chem. Soc. Symposium Series No. 179, Washington D.C., 1982).
- 12) W.W. Wood, Physics of Simple Liquids (North Holland, Amsterdam, 1968).
- 13) D.J. McGinty, J. Chem. Phys. 60, 4733 (1973); W.D. Kristensen, E.J. Jensen and R.M.J. Cotterill, J. Chem. Phys. 60, 4161 (1974).
- 14) E.J. Saletan and A.H. Cromer, "Theoretical Mechanics," Chapter 4 (John Wiley & Sons, Inc. 1971).
- 15) D.S. Schonland, "Molecular Symmetry, An Introduction to Group Theory and Its Uses in Chemistry," Ch. 8 (D. Van Nostrand Company LTD 1965).
- 16) E.E. Polymeropoulos and J. Brickmann, Chem. Phys. Lett. 96, 273 (1983); and 92, 59 (1982).
- 17) I. Oksuz, Surf. Sci., 122, L585 (1982).

- 18) R.D. Etters, L. Kanney, N.S. Gillis and Jaya Kaelberer, Phys. Rev. B 15, 4056 (1977).
- 19) M.R. Hoare, Adv. Chem. Phys. 40, 49 (1979).
- 20) R.C. Baetzold and R.E. Mack, J. Chem. Phys. 62, 1513 (1975).
- 21) S.C. Richtmeier, R.A. Eades, D.A. Dixon and J.L. Gole, Chapter 12 in reference [14]
- 22) A.L. Companion, Chem. Phys. Lett. 56, 500 (1978).
- 23) H.L. Davis and J.R. Noonan, Surf. Sci. 126, 245 (1983).
- 24) H.L. Davis and J.R. Noonan, Surf. Sci. 115, L75 (1982).
- 25) H.L. Davis and J.R. Noonan, J. Vac. Sci. Technol. 20, 842 (1982).
- 26) H.L. Davis, J.R. Noonan and L.H. Jenkins, Surf. Sci. 83, 559 (1979).
- 27) I. Stensgaard, R. Feidenhans'l and J.E. Sorensen, Surf. Sci. 128, 281 (1983).
- 28) D.L. Adams, H.B. Nielsen and J.N. Andersen, Surf. Sci. 128, 294 (1983).
- 29) J.N. Andersen, H.B. Nielsen, L. Petersen and D.L. Adams, J. Phys. C, Solid State Physics 17, 173 (1984).
- 30) D.L. Adams, H.B. Nielsen, J.N. Andersen, I. Stensgaard, R. Feidenhans'l and J.E. Sorensen, Phys. Rev. Lett. 49, 669 (1982).
- 31) E. Bogh and I. Stensgaard, Phys. Lett. 65A, 357 (1978).
- 32) M.W. Finnis and V. Heine, J. Phys. F, Metal Phys. 4, L37 (1974).
- 33) U. Landman, R.N. Hill and M. Mostoller, Phys. Rev. B21, 448 (1980).
- 34) R.N. Barnett, R.G. Berrera, C.L. Cleveland and U. Landman, Phys. Rev. B28, 1667 (1983).
- 35) J.N. Schmit, Surf. Sci. 55, 589 (1976).
- 36) G.C. Benson and T.A. Claxton, J. Phys. Chem. Solids 25, 367 (1964).
- 37) A.R. Miedema, Z. Metallkde. 69, 287 (1978).
- 38) S.Y. Tong and A.L. Maldonado, Surf Sci. 78, 459 (1978).
- 39) F. Jona, H.D. Shih, D.W. Jepsen and P.M. Marcus, J. Phys. C: Solid State Phys. 12, L455 (1979); 10, L67 (1977).

- 40) W.S. Yang, F. Jona and P.M. Marcus, Solid State Comm. 43, 847 (1982).
- 41) J. Ihm, D.H. Lee, J.D. Joannopoulos and A.N. Berker, J. Vac. Sci. Technol. B1, 705 (1983).
- 42) R.E. Schlier and H.E. Farnsworth, J. Chem. Phys. 30, 917 (1959).
- 43) M.T. Yin and M.L. Cohen, Phys. Rev. B 24, 2303 (1981).
- 44) D.J. Chadi and J.R. Chelikowsky, Phys. Rev. B 24, 4892 (1981).
- 45) J.E. Rowe, S.B. Christman and H. Ibach, Phys. Rev. Lett. 34, 874 (1975).
- 46) W.A. Harrison, Surf, Sci. 55, 1 (1976).
- 47) G. Binnig, et al., Phys. Rev. Lett. 50, 120 (1983).
- 48) D.J. Miller and D. Hanneman, J. Vac. Sci. Technol. 16, 1270 (1979).
- 49) L.C. Snyder, Z. Wasserman and J.W. Moskowitz, J. Vac. Sci. Technol. 16, 1266 (1979).
- 50) G.E. Dieter, Mechanical Metallurgy, McGraw-Hill, New York, 1976.
- 51) A. Paskin, A. Gohar and G.J. Jones, Phys. Rev. Lett. 44 (14), 940 (1980).
- 52) W.G. Hoover, A.J.C. Ladd and N.E. Hoover, "Plastic Dislocation Motion via Nonequilibrium Molecular and Continuum Dynamics." In J.K. Lee (ed.), Interatomic Potentials and Crystalline Defects, Proc. Symp. Fall Meet. of the Metallurgical Society of the AIME, Pittsburgh, PA, Oct. 6-7, 1980, Metallurgical Society of AIME, Warrendale, PA, 1981.
- 53) T. Halicioglu and D.M. Cooper, Mat. Sci. Eng. 62, 121 (1984).
- 54) W.T. Ashurst and W.G. Hoover, Phys. Rev. B 14, 1465 (1976).
- 55) G.J. Dienes and A. Paskin, in "Atomistics of Fracture," Ed: R.M. Latanision and J.R. Pickens (Plenum Press, New York, 1983). p. 671.